

Copyright © 1989, by the author(s).
All rights reserved.

Permission to make digital or hard copies of all or part of this work for personal or classroom use is granted without fee provided that copies are not made or distributed for profit or commercial advantage and that copies bear this notice and the full citation on the first page. To copy otherwise, to republish, to post on servers or to redistribute to lists, requires prior specific permission.

**SIMULATION OF TOPOGRAPHY SCATTERING
FOR OPTICAL LITHOGRAPHY WITH THE
CONNECTION MACHINE**

by

John K. Gamelin

Memorandum No. UCB/ERL M89/71

8 June 1989

COVER PAGE

**SIMULATION OF TOPOGRAPHY SCATTERING
FOR OPTICAL LITHOGRAPHY WITH THE
CONNECTION MACHINE**

by

John K. Gamelin

Memorandum No. UCB/ERL M89/71

8 June 1989

ELECTRONICS RESEARCH LABORATORY

College of Engineering
University of California, Berkeley
94720

TITLE PAGE

**SIMULATION OF TOPOGRAPHY SCATTERING
FOR OPTICAL LITHOGRAPHY WITH THE
CONNECTION MACHINE**

by

John K. Gamelin

Memorandum No. UCB/ERL M89/71

8 June 1989

ELECTRONICS RESEARCH LABORATORY

College of Engineering
University of California, Berkeley
94720

Simulation of Topography Scattering for Optical Lithography with the Connection Machine

John K. Gamelin

Department of Electrical Engineering and Computer Sciences
University of California, Berkeley

May 22, 1989

Abstract

A promising new massively parallel technique for rigorous simulation of topography scattering issues in optical lithography has been developed and tested. The method is equivalent to the time-domain finite-difference method (TDFDM) used in electromagnetic scattering, but exploits the parallel nature of wave propagation and the power of recent massively parallel architectures such as the Connection Machine. Efficient new absorbing and periodic boundary conditions are formulated along with rapid techniques for obtaining frequency-domain information. The resulting code has been implemented on a Connection Machine CM-2 and can be applied to analyze general electromagnetic interactions over arbitrarily nonplanar and inhomogeneous topography, both isolated and periodic. Steady-state calculations for a 8.0 wavelength square domain require less than 40 seconds on the 1K processor system at UC Berkeley corresponding to less than 5 seconds on a fully configured 16K (or larger) machine. The accuracy of the method is verified by rigorous integral equation methods for diffraction gratings and SAMPLE for layered dielectric thin films. Several key two-dimensional effects are explored including dynamic exposure over reflective steps and diffraction from latent images in photoresist and contrast enhancement materials. Finally, future extensions to include effects of partial coherence and linking with other simulation programs within a system environment are discussed.

Acknowledgments

I would like to thank my advisor, Professor Andrew Neureuther, for his constant encouragement and contagious excitement throughout this project. I would also like to recognize Dr. Roberto Guerrieri of the Universita' di Bologna, Italy for revealing the secrets of the Connection Machine and collaborating on the early stages of this work. His approach to programming and conceptualizing the problem strongly influenced the growth and development of the method.

Behind any successful venture lie many hard-working colleagues. I would especially like to acknowledge Richard Ferguson for extensively modifying the SAMPLE development routine to generate the profiles shown at the end of this report. Several members of the Deep-UV Lithography group at Berkeley generously devoted many hours of their time to provide helpful and critical discussions. For this and their friendship I would like to thank Gino Addiego, Rich Ferguson, Kenny Toh, Ed Scheckler, Nelson Tam, William Partlo, Don Lyons, Alex Wong, Jaime Ramirez, and Carl Galewski. In this same vein I would like to extend thanks to Don Webber and Andreas Cassoto for their assistance in taming and understanding the Connection Machine. Finally, I extend my deepest thanks to my parents for their never-ending love and support.

The financial support of SEMATECH COE grant 88-MC-500 and the California State MICRO Program grant 88-092 is gratefully acknowledged.

Contents

1	Introduction	1
2	Background for Current Work	4
2.1	Relation to Previous Efforts	4
2.2	Organization of the Connection Machine	6
3	Outline of the Time Domain Algorithm	8
3.1	Statement of the Problem	8
3.2	Spatial and Temporal Discretization ¹	9
3.3	First Order Absorbing Boundary Conditions	11
3.4	Second Order Boundary Conditions	13
3.5	Periodic Boundary Conditions	15
3.6	The Incident Field	17
3.7	Steady-State Formulation	18
4	Implementation on the Connection Machine	22
4.1	Discretization of the Spatial Domain	22
4.2	The Boundary Conditions	22
4.3	The Incident Field	25
5	Special Issues for Topography Scattering in Lithography	27
5.1	Boundary Conditions	27
5.2	Photoresist Bleaching	28

5.3	Highly Conductive Materials	29
6	Tests and Applications	31
6.1	Layered Dielectric Media	31
6.2	Diffraction Gratings	32
6.3	Dynamic Exposure on Flat Substrates	36
6.4	Asymmetry Effects in Alignment	37
6.5	Diffraction from Latent Images	39
6.6	Exposure in Contrast Enhancement Materials	41
6.7	Reflective Notching	43
7	Extensions and Future Work	46
8	Conclusion	50
	References	51
	Figures	55
	Appendix A	80
	Appendix B	82

Chapter 1

Introduction

Over the past few years, three-dimensional (3D) integration of microelectronic devices has forged a new frontier for the semiconductor industry. The unabated push for greater density and higher performance coupled with the limitations of silicon real estate has already stepped beyond the limits of the traditional planar fabrication process. It is clear that future advances will require stacking of device and metallization layers and/or etched features such as trenches. While paving the way for exciting new possibilities for integrated circuit (IC) design, these trends also present tough challenges to both process technologists and computer-aided design (CAD) tools.

In the context of optical lithography, for example, the patterning and alignment of small features over steps and along sidewalls involves complex optical interactions between the exposure (probe) signal, underlying topography, and resonances in the photoresist. Figures 3, 22, and 29 illustrate some of the diverse materials and profiles commonly encountered in present alignment and exposure situations. Current lithography simulation programs such as SAMPLE [1] and PROLITH [2] employ simple quasi-two-dimensional models for exposure based upon the Fresnel equations. These approaches, although computationally efficient, are limited to strictly planar substrates and resist overcoatings. Non-planar topography introduces two-dimensional reflections which require a fundamentally new formulation of the analysis. Furthermore, these models, which assume strict vertical propagation of the image, do not account for diffraction effects produced within the resist itself during the bleaching process. As illustrated in Figure 1, inherent diffraction will play an important role in the formation of latent profiles within the resist, even for flat substrates, as minimum feature sizes are reduced.

This report describes a promising new massively parallel approach to the analysis of electromagnetic scattering from topography in optical lithography. The formulation involves solution of a time-domain discretization of Maxwell's equations similar to a scheme proposed by Yee [3] on a staggered grid of electric and magnetic field nodes. The method has been applied to examine such diverse issues as metrology, alignment, and projection printing over arbitrarily complex topography. The algorithm exploits the inherent parallel nature of wave propagation, making it a perfect match for massively parallel architectures such as the Connection Machine [4]. The combination of the accuracy and flexibility of a finite difference/finite element formulation with the speed of a parallel approach give the technique unique advantages for rigorous simulation unmatched by any other method to date.

Chapter 2 provides some background for the technique by reviewing previous efforts to analyze topography scattering within the context of lithography. An overview of the organization of the Connection Machine, on which the method was implemented, is presented for readers unfamiliar with its advanced architecture. After outlining appropriate simplifications for analysis of typical wafer topographies, Chapter 3 discusses the algorithm in detail. New absorbing boundary conditions, formulated to take advantage of the parallelism of the Connection Machine, are described along with modifications of existing conditions (used in equivalent time domain approaches) to account for propagation in lossy dielectrics. Because periodic structures play an important role in optical lithography, efficient periodic boundary conditions capable of being evaluated in parallel were introduced. These are presented along with new techniques for extracting frequency domain information such as diffraction efficiencies and far-field images.

Chapter 5 treats issues of special concern for topography scattering in lithography such as guiding of waves near boundaries, effects of anomalous dispersion upon stability, and modeling of dynamic bleaching using the Dill [5] relations. The accuracy and remarkable efficiency of the formulation is then verified by comparison with diffraction grating results

from rigorous integral equation methods and dielectric materials using the Fresnel equations and SAMPLE. To demonstrate some of the extensive capabilities of the method. Chapter 6 presents simulations of two-dimensional effects including reflective notching, diffraction in contrast enhancement materials (CEM), and scattering from latent images formed in photoresist during exposure. Finally, important directions for future work to include partial coherence effects and linking with other programs within an integrated simulation framework are examined.

Chapter 2

Background for Current Work

2.1 Relation to Previous Efforts

Optical interactions of interest to lithography can be separated into two classes of problems by the characteristic structure of the topography. The first class deals with periodic structures, typically within the context of metrology and alignment or exposure of repetitive patterns as in memory chips. The second class is concerned with scattering from isolated features on the wafer and the effects upon adjacent devices. For both cases, the steady-state and/or dynamic behavior with illumination may be desired. To handle all of these situations, a simulation tool must be general enough to provide accurate results for domains which may be arbitrarily nonlinear, inhomogeneous, and time-varying with periodic or absorbing boundary conditions. This is an impossible task for any single simulation algorithm. of course, and previous approaches have focused on either periodic or isolated scattering.

Bobroff and Rosenbluth [6] and Gallatin et al. [7] studied diffraction from resist-coated alignment marks (periodic) using plane wave expansions and scattering matrices. Their method, although rapid and efficient, was approximate and limited to long, shallow features with homogeneous layers. Kirk [8], Nyysönen [9], and Yuan et al. [10] developed an improved technique suitable for thick, inhomogeneous periodic structures based upon numerical solution of Hill's equation [11,12]. The algorithm has been used to examine polarization effects in alignment, but instabilities have been observed at short periods. Matsuzawa et al. [13] applied a hybrid finite element/boundary element method to analyze exposure in the vicinity of isolated reflective steps. The method revealed interesting two-dimensional diffraction effects, but required very long computational times and was

restricted to perfectly conducting surfaces.

Wojcik et al. [14] investigated a promising alternative to these traditional frequency domain approaches. The algorithm involves the solution of the coupled, first order Maxwell equations on a uniform rectangular grid superimposed on wafer topography of interest. Wave propagation is achieved by time stepping a finite difference discretization scheme proposed by Yee [3] and absorbing outgoing scattered fields produced by interaction with the features. Good agreement with both theoretical and experimental results was observed for scattering from small ($0.3\text{-}2\mu\text{m}$ diameter) latex spheres on a silicon substrate [14]. Demonstration of the general feasibility of the method was hampered, however, because effective absorbing boundary conditions for the outgoing waves were not found. As a result, grids with over 2.2 million nodes were required, possible only on the CRAY 2 with run times for steady-state calculations of roughly 20 minutes.

The current work develops and extends the time domain finite difference method (TDFDM) introduced by Wojcik et al. The algorithm has been adapted to exploit the inherent parallel nature of wave propagation and execute rapidly and efficiently on new massively parallel computer architectures. Robust absorbing boundary conditions for both free space and dielectric materials have been devised along with new periodic boundary conditions for simulation of periodic structures. Techniques for extracting steady-state information such as diffraction efficiencies and surface currents have also been formulated. The resulting algorithm is now quite general and can be applied to both periodic and isolated structures under pulsed (for frequency response data) or steady-state² excitation.

²Some restrictions upon the numerical aperture of the incident optical signal may be necessary for stability in this case as will be discussed in Section 3.5.

2.2 Organization of the Connection Machine

Before discussing the details of the algorithm, it will be helpful to summarize the architecture and operation of the Connection Machine. This will clarify specific aspects of the implementation and provide a foundation for understanding the suitability of the computer for massively parallel computation.

The Connection Machine is an integrated system consisting of a front end computer and a parallel processing unit containing up to 64K processors with a high-performance data parallel input/output system. Figure 2 depicts the organization of the Connection Machine CM-2. The front end controls the operation of the system by managing the flow of data and instructions to the individual processors while providing a software development environment. Global computations such as data input/output and evaluation of constant expressions are typically executed on the front end while local calculations are sequenced to the processors. Each physical processor supports a simple floating point unit (single or double precision) and 64 Kbit data stack. The system software allows the processors to be configured into sets of n -dimensional grids which can be manipulated individually to carry on different tasks. Communication between sets is possible by means of the *Nexus* of Figure 2 which is a general router based upon a hypercube architecture. The *Nexus* allows every processor to send a message to any other processor, with all messages sent and delivered at the same time [15].

For many applications such as finite element methods and neural network models, local communication between nearest neighbors is sufficient. For these purposes, the Connection Machine supports a more structured and faster method called the *NEWS grid* in which processors can pass data along a fixed rectangular pattern. For example, in a two-dimensional grid each processor could send and receive data from neighbors n units to the north, south, east, west or any combination thereof. The data is automatically wrapped around to the other side if the coordinates extend beyond the current boundaries.

When more computational units are required than the physical configuration, *virtual* processors are created which share the arithmetic-logic units (ALU) and memory of the available processors. The CM-2 requires allocation of at least 1 Kbit stack for each virtual processor allowing up to 4096K nodes for calculations. In practice, however, memory considerations for each computational node (algorithm dependent) may limit the virtual-to-physical processor (VP) ratio to 32 or less. To get a feel for the potential performance of the system, a fully configured CM-2 with 64K processors and VP ratio of 32, each performing a single-precision floating point multiplication, operates at about 4000 MFlops including all instruction issuing and overhead [15]. The prototype CM-2 installed at Berkeley and used for simulations in this work has 1K physical processors and can be operated at VP ratios of up to 64 (periodic) and 32 (isolated) with the indicated versions of the algorithm.

Chapter 3

Outline of the Time Domain Algorithm

3.1 Statement of the Problem

Figure 3 illustrates a typical simulation domain for optical lithography as might be encountered in alignment. The problem to be solved is the classical Maxwell's equations which can be stated as follows:

$$\nabla \times \vec{H} = \frac{\partial \vec{D}}{\partial t} + \vec{J} \quad (1)$$

$$\nabla \times \vec{E} = -\frac{\partial \vec{B}}{\partial t} \quad (2)$$

supplemented with the relations:

$$\vec{D} = \epsilon \vec{E} \quad (3)$$

$$\vec{B} = \mu \vec{H} \quad (4)$$

$$\vec{J} = \sigma \vec{E} \quad (5)$$

where ϵ and μ are the dielectric constant and the permeability of the material. Using Stokes's theorem, equations (1) and (2) can be written in integral form as:

$$\oint_l \vec{H} \cdot \hat{i} dl = \int_S \left\{ \frac{\partial \vec{D}}{\partial t} + \vec{J} \right\} \cdot \hat{n} dS \quad (6)$$

$$\oint_l \vec{E} \cdot \hat{i} dl = - \int_S \frac{\partial \vec{B}}{\partial t} \cdot \hat{n} dS \quad (7)$$

For the cases considered in this work, a two-dimensional domain with a linearly polarized incident transverse electric (TE) plane wave has been assumed to simplify the analysis.

Under these conditions the relevant field components are the following:

$$\vec{E} = \{0, 0, E_z\} \quad (8)$$

$$\vec{H} = \{H_x, H_y, 0\} \quad (9)$$

Extension of the results to incident transverse magnetic (TM) modes and three dimensions is straightforward and can be formulated in analogy with similar treatments elsewhere [3.16].

Since the electric field is always parallel to the discontinuities of the dielectric constants and since the magnetic permeability is constant all over the domain, each field component is continuous everywhere. For TM modes this is not true and proper averaging of the local dielectric constants is necessary. Referring to Figure 3, the boundary conditions can be stated as follows: given a rectangular domain bounded by points A, B, C, and D, the boundary conditions along A-B and C-D are of the absorbing type while those along A-D and B-C can be either periodic or absorbing. We further assume that the incident field reaches the structure along the line C-D at an arbitrary angle.

3.2 Spatial and Temporal Discretization³

In the TDFDM developed by Yee, the electric and magnetic fields are calculated using a staggered grid in which each field component occupies a distinct node. Electric field components are mapped to lattice points with integral coordinates (i,j,k) while magnetic field values reside at half-integral coordinates {e.g. (i±1/2,j,k)}. In analogy, Figure 4 depicts a uniform grid appropriate for two-dimensional domains. It can be shown that this discretization follows directly from an expansion of the fields onto a piecewise-constant orthogonal basis. A corresponding finite element method has been devised in which polynomial interpolation functions are used for a more accurate and conformal representation of the fields [17]. Further discussions of this technique can be found in [18].

Applying this discretization scheme to equations (3) through (7), following Figure 5 we

³The author is indebted to Dr. Roberto Guerrieri of the Universita' di Bologna, Italy for deriving and phrasing many of the results of this section in a collaborative research effort while on sabbatical at U. C. Berkeley in 1988.

obtain:

$$(H_x(i, j - 1/2) - H_x(i, j + 1/2) + H_y(i + 1/2, j) - H_y(i - 1/2, j))h = \quad (10)$$

$$h^2 \left(\epsilon \frac{\partial E_z(i, j)}{\partial t} + \sigma E_z \right)$$

$$(E_z(i, j + 1) - E_z(i, j)) = -h\mu \left(\frac{\partial H_x(i, j + 1/2)}{\partial t} \right) \quad (11)$$

$$(E_z(i, j) - E_z(i + 1, j)) = -h\mu \left(\frac{\partial H_y(i + 1/2, j)}{\partial t} \right) \quad (12)$$

where E_z, H_x, H_y are continuous functions of time t and h is the discretization step. The accuracy of this scheme increases proportional to h^2 when the domain is smooth.

To obtain a suitable discretization of the time dependency of equations (10, 11, 12), it is possible to integrate again (10, 11, 12) in the time domain:

$$h \int_{t_n}^{t_{n+1}} (H_x(i, j - 1/2) - H_x(i, j + 1/2) + H_y(i + 1/2, j) - H_y(i - 1/2, j)) dt = \quad (13)$$

$$h^2 \int_{t_n}^{t_{n+1}} \left(\epsilon \frac{\partial E_z(i, j)}{\partial t} + \sigma E_z(i, j) \right) dt$$

which gives:

$$\frac{h}{\Delta t} \epsilon (E_z^{n+1}(i, j) - E_z^n(i, j)) + \frac{h\sigma}{2} (E_z^{n+1}(i, j) + E_z^n(i, j)) = \quad (14)$$

$$H_x^{n+1/2}(i, j - 1/2) - H_x^{n+1/2}(i, j + 1/2) + H_y^{n+1/2}(i + 1/2, j) - H_y^{n+1/2}(i - 1/2, j)$$

which can be rewritten as:

$$E_z^{n+1}(i, j) = \alpha E_z^n(i, j) \quad (15)$$

$$+ \beta (H_x^{n+1/2}(i, j - 1/2) - H_x^{n+1/2}(i, j + 1/2) + H_y^{n+1/2}(i + 1/2, j) - H_y^{n+1/2}(i - 1/2, j))$$

where $n, n + 1/2$ and $n + 1$ refer to an integration interval of length Δt , α is defined as

$$\alpha = \frac{h\epsilon/\Delta t - h\sigma/2}{h\epsilon/\Delta t + h\sigma/2}$$

$$\beta = \frac{1}{h\epsilon/\Delta t + h\sigma/2}$$

and the magnetic field has been evaluated at a midpoint of the integration interval. Again it is easy to see that the local truncation error is of the order of h^2 . The remaining equations are:

$$H_x^{n+1/2}(i, j + 1/2) = H_x^{n-1/2}(i, j + 1/2) + \frac{\Delta t}{h\mu} (E_z^n(i, j) - E_z^n(i, j + 1)) \quad (16)$$

$$H_y^{n+1/2}(i + 1/2, j) = H_y^{n-1/2}(i + 1/2, j) + \frac{\Delta t}{h\mu} (E_z^n(i + 1, j) - E_z^n(i, j)) \quad (17)$$

which provide a complete discretization of the problem at internal points. The above discretization is equivalent to the finite difference scheme proposed by Yee which was derived following a different procedure.

For algorithmic stability, the time and spatial steps Δt and h must be related by the Courant condition [19]:

$$v_{max} \Delta t \leq \frac{h}{\sqrt{2}} \quad (18)$$

where v_{max} is the maximum phase velocity within the domain (c/n where n is the largest index of refraction). To be precise, the Courant condition is actually a conservative limit to guarantee convergence. Time steps up to $\sqrt{2}$ larger than the limit have been shown to yield stable results for simple scatterers such as layered dielectrics. Typically, h is chosen so that there are at least 10 nodes/ λ in the largest index material within the domain with 15-20 nodes/ λ being the most common usage.

3.3 First Order Absorbing Boundary Conditions

Although many absorbing boundary conditions have been proposed in the literature, most are not well suited for parallel computation. In order to reduce the time spent updating boundary nodes, it is desirable to formulate conditions which resemble operations performed within the domain as closely as possible. A physically intuitive way of deriving one such condition proceeds as follows. Suppose we want to evaluate the electric field $E_z(0, j)$ of Figure 6. Because the mesh has been terminated, however, $H_y(-1/2, j)$ is not known. If

the outgoing scattered field were a plane wave propagating at an angle θ with respect to the boundary normal, H_y would be related to the local E_z by

$$E_z = (\eta \cos \theta) H_y \quad (19)$$

where η is the medium impedance defined as $\sqrt{\mu/\epsilon}$. This suggests a means for calculating $E_z(0, j)$ using only interior fields. Approximating $E_z(0, j)$ by $E_z(0.25, j)$ and integrating (6) along the rectangular path shown within the domain and using (19) for H_y we obtain an equation valid for a node on the boundary:

$$\begin{aligned} \frac{h^2}{2\Delta t} \epsilon (E_z^{n+1}(0, j) - E_z^n(0, j)) + \frac{h^2 \sigma}{4} (E_z^{n+1}(0, j) + E_z^n(0, j)) = \\ \frac{h}{2} (H_x^{n+1/2}(0, j - 1/2) - H_x^{n+1/2}(0, j + 1/2)) + h H_y^{n+1/2}(1/2, j) - \\ \frac{h}{2\eta \cos \theta} (E_z^{n+1}(0, j) + E_z^n(0, j)) \end{aligned} \quad (20)$$

This can be rewritten in the more convenient form:

$$\begin{aligned} E_z^{n+1}(0, j) = \bar{\alpha} E_z^n(0, j) \\ + \bar{\beta} (H_x^{n+1/2}(0, j - 1/2) - H_x^{n+1/2}(0, j + 1/2) + 2H_y^{n+1/2}(1/2, j)) \end{aligned} \quad (21)$$

where

$$\begin{aligned} \bar{\alpha} &= \frac{h^2 \epsilon / 2\Delta t - h^2 \sigma / 4 - h / (2\eta \cos \theta)}{h^2 \epsilon / 2\Delta t + h^2 \sigma / 4 + h / (2\eta \cos \theta)} \\ \bar{\beta} &= \frac{h/2}{h^2 \epsilon / 2\Delta t + h^2 \sigma / 4 + h / (2\eta \cos \theta)} \end{aligned}$$

A similar equation can be written for the south boundary with the substitutions $H_y^{n+1/2}(1/2, j) \rightarrow -H_y^{n+1/2}(N_x - 1/2, j)$ and $i = 0 \rightarrow i = N_x$ where N_x represents the number of nodes in the x dimension. Note that this equation closely resembles (15) except for the forms of the constants and the coefficients of the H_y contributions. Similar relations can be derived using other integration paths, but (21) has proven to be simple and efficient.

For lossy dielectric materials, η is complex and (19) cannot be applied correctly in the time domain since the imaginary component of η introduces a phase shift ϕ between the

two fields:

$$\tan(\phi) = \frac{\sigma}{2\omega\epsilon_r}$$

where ϵ_r is the real part of the dielectric constant. Nevertheless, fairly good results have been obtained for normal incidence as will be discussed later.

3.4 Second Order Boundary Conditions

The absorbing boundary condition outlined in the previous section allows maximum parallelism, but only absorbs incident plane waves from a single angle of incidence. This typically produces unacceptable errors when analyzing structures with high aspect ratio which can scatter into several plane wave modes with nearly equal efficiency. Second order boundary conditions, which absorb plane waves from two angles of incidence simultaneously have been found through extensive studies on diffraction gratings to yield much better results. This is particularly true when the angles of incidence for absorption are unknown prior to computation or when the waves graze the boundary ($\theta_{inc} \approx 90^\circ$).

Mur [20] has developed second order conditions which provide stable, broad angle absorption with excellent efficiency and low memory requirements. Complete discussions of these and equivalent conditions are given in references [21,22,23]. Modifying the treatment by Mur to account for (potentially lossy) dielectrics, factorization of the wave equation yields a boundary operator for an outgoing scattered wave propagating in the $-x$ direction:

$$(\partial_x - i\omega\sqrt{\mu\epsilon_c}) E_z |_{x=0} = \left(\partial_x - i\frac{\omega n_c}{c_0} \right) E_z |_{x=0} \simeq 0 \quad (22)$$

where ϵ_c and $n_c = n - ik$ are the complex dielectric constant and index of refraction respectively, and c_0 is the speed of light in vacuum. Assuming a solution of the following form:

$$E_z = \underbrace{E_0(y)e^{i\omega(t+nx/c_0)}}_{E_1(x,y,t)} e^{\overbrace{(\omega k/c_0)x}^a} \quad (23)$$

leads to an equivalent operator valid in the time domain involving only real quantities:

$$\left(\partial_x - \frac{n}{c_0} \partial_t\right) E_1(x, y, t) |_{x=0} \simeq 0 \quad (24)$$

In effect, the transformation (23) accounts for attenuation of the wave as it approaches the boundary. For pulsed excitation, dispersion must be directly incorporated into the boundary operator.

Proceeding using the central differencing of Mur, two-dimensional equations for the north (C-D), south (A-B), east (B-C), and west (A-D) boundaries, respectively, can be written:

$$\begin{aligned} E_z^{n+1}(0, j) &= e^{-\alpha h} E_z^n(1, j) + c_1 \left[e^{-\alpha h} E_z^{n+1}(1, j) - E_z^n(0, j) \right] \\ &\quad - c_2 \left[H_x^{n+1/2}(0, j + 1/2) - H_x^{n+1/2}(0, j - 1/2) \right. \\ &\quad \left. + e^{-\alpha h} \left(H_x^{n+1/2}(1, j + 1/2) - H_x^{n+1/2}(1, j - 1/2) \right) \right] \end{aligned} \quad (25)$$

$$\begin{aligned} E_z^{n+1}(N_x, j) &= e^{-\alpha h} E_z^n(N_x - 1, j) + c_1 \left[e^{-\alpha h} E_z^{n+1}(N_x - 1, j) - E_z^n(N_x, j) \right] \\ &\quad - c_2 \left[H_x^{n+1/2}(N_x, j + 1/2) - H_x^{n+1/2}(N_x, j - 1/2) \right. \\ &\quad \left. + e^{-\alpha h} \left(H_x^{n+1/2}(N_x - 1, j + 1/2) - H_x^{n+1/2}(N_x - 1, j - 1/2) \right) \right] \end{aligned} \quad (26)$$

$$\begin{aligned} E_z^{n+1}(i, 0) &= e^{-\alpha h} E_z^n(i, 1) + c_1 \left[e^{-\alpha h} E_z^{n+1}(i, 1) - E_z^n(i, 0) \right] \\ &\quad - c_2 \left[H_y^{n+1/2}(i - 1/2, 0) - H_y^{n+1/2}(i + 1/2, 0) \right. \\ &\quad \left. + e^{-\alpha h} \left(H_y^{n+1/2}(i - 1/2, 1) - H_y^{n+1/2}(i + 1/2, 1) \right) \right] \end{aligned} \quad (27)$$

$$\begin{aligned} E_z^{n+1}(i, N_y) &= e^{-\alpha h} E_z^n(i, N_y - 1) + c_1 \left[e^{-\alpha h} E_z^{n+1}(i, N_y - 1) - E_z^n(i, N_y) \right] \\ &\quad - c_2 \left[H_y^{n+1/2}(i - 1/2, N_y) - H_y^{n+1/2}(i + 1/2, N_y) \right. \\ &\quad \left. + e^{-\alpha h} \left(H_y^{n+1/2}(i - 1/2, N_y - 1) - H_y^{n+1/2}(i + 1/2, N_y - 1) \right) \right] \end{aligned} \quad (28)$$

where all fields correspond to the *scattered* values and

$$c_1 = \frac{c \Delta t - n h}{c \Delta t + n h}$$

$$c_2 = \frac{\mu_0 c h}{2(c \Delta t + n h)}$$

At the interfaces between two materials, the choice of a proper n is unclear because an outgoing wave is actually a guided mode not well represented by a sum of plane waves. Several possibilities which have been implemented are the average index

$$n_{eff} = \frac{n_1 + n_2}{2}$$

the root-mean-square (RMS) index,

$$n_{eff} = \sqrt{\frac{n_1^2 + n_2^2}{2}}$$

and the index corresponding to the RMS velocity,

$$n_{eff} = \frac{1}{\sqrt{\frac{1}{n_1^2} + \frac{1}{n_2^2}}}$$

In many cases, it is desirable to keep track of the total fields to avoid unnecessary modifications of the computations for inner nodes. Substituting $E_z^{scat} = E_z^{total} - E_z^{inc}$ and the analogous relations for the magnetic fields in equation (28), for example, we can update the boundary nodes using the total and incident fields by

$$\begin{aligned} E_z^{n+1} = & [28]_{scat \rightarrow total} + (1 - c_1) [E_{z,inc}^{n+1}(i) - E_{z,inc}^n(i)] \\ & + 2 c_2 [H_{y,inc}^{n+1/2}(i + 1/2) - H_{y,inc}^{n+1/2}(i - 1/2)] \end{aligned} \quad (29)$$

for the special case of a normally incident plane wave (such that fields with the same x coordinate are equal) and $\alpha = 0$. The incident fields can be computed analytically or numerically in parallel. Specific details are discussed in Section 4.2.

3.5 Periodic Boundary Conditions

In periodic structures, the fields at points spaced one period d apart differ only by a phase shift $\phi = k_i^{inc} d_i$ where k_i and d_i represent the propagation constant and period, respectively.

of the *incident* field in the dimension of periodicity i (Floquet condition). This relation, due to time delays for the incident field to reach each period “cell” and coupling between cells, requires a special treatment of the side (east/west) boundaries. Consider an incident plane wave at the north-western corner of the domain as illustrated in Figure 7. For a normally incident plane wave $\theta_{inc} = 0^\circ$,

$$\phi = \left(\frac{2\pi}{\lambda} \sin(\theta_{inc}) \right) d_i = 0^\circ$$

so that each node point on the east boundary is in synchronization with the corresponding node on the west face. In this case, the boundary nodes can be treated as an interior node with the missing field component supplied from the node on the opposite side of the domain for a considerable savings in execution time. At the same time, errors due to the absorbing conditions are eliminated.

For arbitrary angles of incidence, the periodic conditions cannot be implemented correctly using a *numerical* method as can be seen from Figure 7. Fields on the eastern boundary require delayed values of the field on the western boundary. In the time domain, the phase shift (for a sinusoidal excitation) can be approximated by an equivalent time delay

$$N_d \Delta t \simeq \frac{k_x d_x}{\omega} \quad (30)$$

Conversely, nodes on the western boundary require time *advanced* values of the fields on the eastern face which are not known due to the causality inherent in the time domain method. A possible method to sidestep this problem, which has not been fully tested, follows from the fact that in steady-state the fields for a sinusoidal source must also be sinusoidal. Thus a time advance of

$$N_d \Delta t \simeq \frac{k_x d_x}{\omega}$$

is equivalent to a time delay of

$$N_a \Delta t = (N - N_d) \Delta t \quad (31)$$

where

$$N = \frac{k_{inc} h}{\omega} = \frac{2\pi h}{\lambda_0 \omega}$$

is the number of time increments in a single cycle of the incident field. The delayed fields should not be passed to the boundary nodes until N_d time steps after the field reaches the corresponding node on the opposite boundary. Since this approximation is valid only in steady-state, it may cause instabilities during the transient and limit the maximum angle of incidence.

For many situations of interest to lithography, the need to *directly* simulate scattering using off-axis signals can be relaxed if the incident aerial image is near focus. In that case, the *composite* image locally behaves like normally incident signal and the $\theta_{inc} = 0^\circ$ periodic conditions are appropriate. These points are examined further in Section 6.5.

3.6 The Incident Field

The absorbing boundary conditions discussed in the previous sections with the exception of equation (29) must be applied directly to the scattered field. Greater accuracy can be achieved, however, if the total fields are computed, especially in very lossy materials where the scattered and incident fields almost cancel [19]. In order to avoid costly conversions at each time step, the field components at the outermost nodes (e.g. E_z and H_x on the north) are represented in terms of the scattered values throughout the computation. When updating the fields on the boundary, the incident fields for the adjacent nodes are subtracted from the total values. Conversely, the incident field for the boundary nodes is added to the scattered values to compute the fields in the adjacent layer. This distinction of roles increases the efficiency of the boundary conditions while providing an immediate knowledge of the scattered fields for far-field calculations.

The proper incident field for steady-state calculations is typically a sinusoidal plane wave (possibly modulated by an image from a mask). Care must be observed in applying

the fields because the scattered field near the source is sensitive to synchronization errors between the numerical propagation on the grid and the analytic incident field. This can contribute noticeable discrepancies for domains with low diffraction efficiencies. To reduce errors produced by introducing the source abruptly at $t=0$, a gaussian tail can be applied before starting the sinusoidal excitation. The three parameters A , t_0 , and T associated with the gaussian

$$A \exp \left[-\left(\frac{t - t_0}{T} \right)^2 \right]$$

are used to match the (1) field and (2) its time derivative at $t = N_0 \Delta t$ and (3) set the initial value (e.g. $E_z \leq 10^{-10} = \beta$). For a $\sin(\omega t)$ source, the parameters are related by

$$t_0 = \frac{a(N_0 \Delta t)^2 + b(N_0 \Delta t)}{2a(N_0 \Delta t) + b} \quad (32)$$

$$T = \sqrt{\frac{n \Delta t - t_0}{a}} \quad (33)$$

$$A = \beta \exp \left[\left(\frac{t_0}{T} \right)^2 \right] \quad (34)$$

where

$$a = -\frac{\omega}{2} \cot(\omega \Delta t)$$

$$b = \ln \left[\frac{\sin(\omega \Delta t)}{\beta} \right]$$

and N_0 is the number of time steps the gaussian is applied before introducing the sinusoid.

3.7 Steady-State Formulation

One advantage of a time domain approach to the solution of scattering problems is that the effect of multiple frequencies can be determined by studying the response of the system to a single pulse. At the same time, however, single frequency (monochromatic) information can be found by using a continuous sinusoidal source and stepping the response until the fields become periodic with the source frequency. Several methods for testing this condition are possible including use of the Discrete Fourier Transform (DFT). The simplest technique

involves waiting until the first reflections from the structure arrive at the north boundary. then computing the mean-square error (MSE) along a cut-line ($x = \text{constant}$) between the current fields $\{t = n\Delta t\}$ and those from the previous period $\{t = (n - N)\Delta t\}$. Steady-state is achieved when the error falls below a specified tolerance for three consecutive cycles. If convergence is not reached the algorithm is stepped through another period ($N\Delta t$) and tested again.

As outlined in Appendix A, once the fields have reached steady-state the appropriate diffraction efficiencies for outgoing modes in periodic structures can be calculated. Expanding the scattered field in outgoing harmonics,

$$f_s(\vec{r}, t) = \sum_n \left\{ A_n \cos(\omega t - \vec{k}_n \cdot \vec{r}) + B_n \sin(\omega t - \vec{k}_n \cdot \vec{r}) \right\} \quad (35)$$

and defining two times t_1 and t_2 such that $\cos(\omega t_1) = 0$ and $\sin(\omega t_2) = 0$, the coefficients can be determined from the following:

$$A_{\pm m} = \frac{1}{d} [\gamma_{22} \pm \gamma_{11}] \quad (36)$$

$$B_{\pm m} = \frac{1}{d} [\gamma_{12} \mp \gamma_{21}] \quad (37)$$

where using the convention of Figure 3 with d denoting the periodicity and f_s the scattered field at the top boundary,

$$\gamma_{ij} = \int_{C-D} f_s(\vec{r}, t_i) \left\{ \begin{array}{l} \sin(\vec{k}_m \cdot \vec{r}) \quad j = 1 \\ \cos(\vec{k}_m \cdot \vec{r}) \quad j = 2 \end{array} \right\} dy \quad (38)$$

The far-field can thus be reconstructed from simple integrals of the scattered field along boundary C-D at two time instants using (35). The diffraction efficiencies follow immediately:

$$D_m = (A_m^2 + B_m^2) \cos \theta_m \quad (39)$$

$$\angle D_m = \arctan \left[\frac{B_m}{A_m} \right] \quad (40)$$

where θ_m is the angle with the normal for the m th mode

$$\theta_m = \arccos \frac{k_{mx}}{k}$$

The accuracy of the diffraction efficiency calculations depends upon the proximity of C-D to the top layer of the scatterer and the discretization (which determines the accuracy of the integrations and the resolution of t_1 and t_2).

In optical lithography one is often interested in through-the-lens alignment schemes in which the wafer topography is illuminated by a projected pattern and the scattered light collected by a detector. For these situations, the image as received by a detector is more useful. The intensity at the image plane, assuming perfect imaging (neglecting lens effects), is simply given by the normal component of the Poynting vector $\vec{S} = \vec{E} \times \vec{H}$ which using (35) and averaging over time is

$$\begin{aligned} I_{norm}(y) &= \vec{S} \cdot (-\hat{x}) \\ &= \frac{1}{2\eta_0} \sum_{l,n} \cos(\theta_n) \left\{ (A_l A_n + B_l B_n) \cos \left[(\vec{k}_n - \vec{k}_l) \cdot \vec{r} \right] \right. \\ &\quad \left. + (A_n B_l - A_l B_n) \sin \left[(\vec{k}_n - \vec{k}_l) \cdot \vec{r} \right] \right\} \end{aligned} \quad (41)$$

Notice that numerical evaluation of this expression requires specification of an image plane height, but the result is independent of the convention so $x = 0$ can be assumed. Alternatively, the image can be calculated directly by integrating the field values for the nodes on the top boundary (scattered field) over a period of the incident field $\{N_t \text{ points}\}$:

$$I(y) = \frac{1}{2N_t} \sum_{j=0}^{N_t-1} E_z^n(0, j) \left[H_y^{n-1/2}(1/2, j) + H_y^{n+1/2}(1/2, j) \right] \quad (42)$$

This method introduces some error since H_y is not known at $x = 0$, but can be carried out very rapidly on the Connection Machine. The largest numbered harmonics N_h (both positive and negative) which need to be calculated is determined by the numerical aperture of the imaging (NA_i) and collection (NA_c) lenses by the following:

$$NA_i = \left| NA_c + N_h \frac{\lambda}{d} \right| \quad (43)$$

which follows from Floquet's theorem.

$\mu = \mu + 2\pi i n$

where n is an integer.

Let μ be a root of the characteristic equation

of the system (1). Then μ is a root of the characteristic equation of the system (2) if and only if μ is a root of the characteristic equation of the system (3). This is because the characteristic equation of the system (1) is $\det(A - \mu I) = 0$, the characteristic equation of the system (2) is $\det(B - \mu I) = 0$, and the characteristic equation of the system (3) is $\det(C - \mu I) = 0$. Since A, B, C are related by $A = B + C$, it follows that $\det(A - \mu I) = \det(B - \mu I) + \det(C - \mu I)$. Therefore, if μ is a root of the characteristic equation of the system (1), then μ is a root of the characteristic equation of the system (2) if and only if μ is a root of the characteristic equation of the system (3).

Let μ be a root of the characteristic equation of the system (1).

Then μ is a root of the characteristic equation of the system (2) if and only if μ is a root of the characteristic equation of the system (3). This is because the characteristic equation of the system (1) is $\det(A - \mu I) = 0$, the characteristic equation of the system (2) is $\det(B - \mu I) = 0$, and the characteristic equation of the system (3) is $\det(C - \mu I) = 0$. Since A, B, C are related by $A = B + C$, it follows that $\det(A - \mu I) = \det(B - \mu I) + \det(C - \mu I)$. Therefore, if μ is a root of the characteristic equation of the system (1), then μ is a root of the characteristic equation of the system (2) if and only if μ is a root of the characteristic equation of the system (3).

Let μ be a root of the characteristic equation of the system (1).

Then μ is a root of the characteristic equation of the system (2) if and only if μ is a root of the characteristic equation of the system (3). This is because the characteristic equation of the system (1) is $\det(A - \mu I) = 0$, the characteristic equation of the system (2) is $\det(B - \mu I) = 0$, and the characteristic equation of the system (3) is $\det(C - \mu I) = 0$. Since A, B, C are related by $A = B + C$, it follows that $\det(A - \mu I) = \det(B - \mu I) + \det(C - \mu I)$. Therefore, if μ is a root of the characteristic equation of the system (1), then μ is a root of the characteristic equation of the system (2) if and only if μ is a root of the characteristic equation of the system (3).

Chapter 4

Implementation on the Connection Machine

4.1 Discretization of the Spatial Domain

Inspection of the above algorithm shows that the staggering of the electric and magnetic field components in both time and space allows each component of the magnetic field to be evaluated in parallel. Once these values are known, the electric field can be updated in a similar fashion. This consideration suggests the allocation of three variables E_z , H_x , and H_y to each processor. This is illustrated by the dashed box in Figure 4. In this way a processor is kept active computing the new values of the unknowns at each time step. To reduce memory requirements in the implementation, the three unknowns were assumed to share common dielectric properties. Fortunately, no error is introduced by this simplification for the TE case since ϵ and σ only enter the equation for E_z .

In keeping with the uniform grid of the finite difference scheme, the input framework was purposely kept simple. The boundaries are specified in piecewise-linear fashion $\{(x,y)$ coordinates with linear interpolation in between} and scanned from AD to BC. The processors corresponding to nodes below each layer boundary are loaded in parallel with the appropriate constants α and β or $\{\bar{\alpha}, \bar{\beta}\}$, $\{c_1, c_2\}$. This method is flexible enough to handle buried structures such as polysilicon or aluminum lines.

4.2 The Boundary Conditions

Special care is required when dealing with the nodes associated with the boundary conditions. Note that the absorbing methods described earlier were obtained for boundary electric fields. Field components outside the domain (e.g. H_y on the south and H_x on the

west—see Figure 4) should be ignored during the simulation unless new relations are derived. We treat each boundary condition in turn.

First Order Conditions

Examination of equations (21) and (15) indicates that formal substitution of $-H_y^{n+1/2}(1/2, j)$ for $H_y^{n+1/2}(-1/2, j)$ in the latter results in equivalent equations. This reordering of variables can be achieved efficiently by allocating an additional row (or column) adjacent to the boundary rows (columns). This “dummy layer” can be used as scratch memory to store and replace the appropriate values. For example, before updating E_z the dummy processors on the north [south] could retrieve $H_y^{n+1/2}(1/2, j)$ [$H_y^{n+1/2}(N_x - 1/2, j)$] computed at the previous half time step and store the sign-reversed value in its own H_y variable. Then E_z could be computed using equation (15) for the *entire domain*. The cost involved in this boundary condition is thus a single-local communication which makes it extremely efficient. In addition to simplifying the organization of the calculation, the allocation of dummy processors avoids the need to allocate extra memory into the “internal” processors. For a single-instruction multiple-data (SIMD) parallel architecture such as the Connection Machine, the memory would have to be allocated to all processors regardless of whether the variables are used or not.

Second Order Conditions

The second order conditions are 30-40% more costly to implement than the first order conditions due to the increased communication with nearby processors and lack of similarity with the algorithm for internal nodes. Another consideration is the computation of the incident fields for the outermost two nodes at each boundary. Consider equation (28). For a normally incident plane wave $E_z, H_y, 0$, the incident field at each time step must be computed for both the electric and magnetic fields to update the boundary node. This can

be accomplished by allocating a set of dummy layers to compute and store the appropriate fields. If the incident wave is not normally incident, however, seven distinct quantities must be tracked: 3 E_z 's and 4 H_y 's. To avoid allocation of new variables, several dummy layers can be added, but not without with a severe communications penalty. To put this into perspective, recent tests with version 5.0 of the Connection Machine *Lisp software indicate that nearest-neighbor communications may be equivalent to almost 3 floating point operations (FLOPs). Assuming communications across a few nodes with the router scale almost linearly with distance, a single fetch for an incident field along the boundary may cost nearly 10 FLOPs. Further, most of the processors are inactive during this time, lowering efficiency.

For normally incident fields, however, the scheme is quite efficient as can be observed from equation (29). Since $H_x = 0$ the incident fields can be computed in a single vertical dummy layer using the same operations as interior nodes. *A note of caution:* For the east and west boundaries, the incident field grazes the surface ($\theta_{inc} = 0^\circ$) and can induce an H_x component because the conditions are designed to absorb waves propagating normal to the side. This effect can be reduced significantly by considering the *incident field* to be the one-dimensional *scattered* field due to the topography at the boundaries. Any normal component H_x which arises will then be due to scattering from topography within the domain. We are free to separate the incident/scattered components as we choose as long as the computations are kept consistent. In practice as small H_x is induced even with the above correction due to the finite roundoff error associated with single-precision operations.

Periodic Boundary Conditions

With periodic boundary conditions and normal incidence, the fields can be "wrapped" around the domain using the *NEWS* grid function discussed earlier. For non-normal incidence, however, the problem of time delayed and time advanced fields must be treated. A

simple and efficient means for accomplishing this is as follows:

- propagate the incident field from the northwest or northeast corners of the domain as appropriate. Dummy layers on the north and west (east) are used to “feed” the boundary nodes as the field reaches each corresponding node. Before the field arrives at each point, the appropriate dummy nodes are masked.
- allocate an extra variable in each processor to serve as a delay line for the boundary nodes. At each time step, the delayed fields are shifted toward the appropriate boundary using local communications. See Figure 7.
- when the first edges of the incident wavefronts reach the scatterer, the excitation along the sides is shut off and the normal side boundary conditions activated (with the delays).
- normal propagation is continued until steady-state achieved.

Preliminary tests have shown this method to be stable for simple topography, but with incorrect results. The fields appear to reflect or superimpose along the non-excited side of the boundary and add a large (80%) ripple along the wavefronts. A simple sign error may account for the problems.

4.3 The Incident Field

The incident electric field can be represented as

$$E_z(x, y; t) = A \sin(\omega t - \vec{k} \cdot \vec{r}) = A \Im \left(e^{i(\omega t - \vec{k} \cdot \vec{r})} \right) \quad (44)$$

which can be evaluated rapidly by calculating and storing the spatial phase factor $e^{-\vec{k} \cdot \vec{r}}$ in each processor within the dummy layers. At each time step the field is updated by multiplication with $e^{i\omega\Delta t}$ (stored on the host computer). This requires four multiplications and

two additions and avoids the computation of trigonometric functions which are expensive to evaluate at run time.

Because the fields within the domain to which the incident field must be added are calculated numerically, there is some dispersions of the propagation constant from the analytic expression $k = 2\pi/\lambda_0$. The exact result depends upon the discretization algorithm. but for equations (15) - (17) the appropriate value in agreement with [24] is given by

$$k = \frac{2}{h} \arcsin \left[\frac{n_0 h \sin \left(\frac{1}{2} \omega \Delta t \right)}{c \Delta t} \right] \quad (45)$$

Chapter 5

Special Issues for

Topography Scattering in Lithography

Simulation of topography scattering for lithography involves special considerations not encountered in usual time domain scattering studies such as dielectrics at absorbing boundaries, dynamic changes in material properties, and media with anomalous dispersion.

5.1 Boundary Conditions

The presence of dielectrics at absorbing boundaries complicates the usual application of outgoing wave conditions. For example, as discussed in Section 4.2, reflections of the incident field from the layers along the side boundaries introduces a *scattered* field component parallel to sides A-D and B-C. The absorbing conditions, however, are optimized for normal incidence and can produce errors if the incident and scattered fields are not reinterpreted to remove this contribution. Another point, considered in Section 3.4, is the inadequacy of representing scattered fields along the dielectric side boundaries as a sum of outward traveling plane waves with a unique velocity. The waves at these boundaries are actually guided when dielectrics are present with propagation constants which are feature-dependent. All scattering studies to date which use absorbing boundary conditions have assumed free-space along the boundaries. This situation clearly does not apply to structures on semiconductor substrates. Research with some bearing on this problem has been conducted for the analysis of propagation characteristics of planar microstrips using a time-domain method [25]. In these studies, however, the researchers noted that proper absorbing conditions were unavailable leading to errors on the order of 5-10%.

5.2 Photoresist Bleaching

Optical properties of nonlinear materials such as photoresist are typically specified in terms of complex indexes of refraction instead of the dielectric constant and conductivity of Maxwell's equations. The complex index of refraction \tilde{n} is defined by

$$\tilde{n} = n - ik$$

where n is the real index of refraction (used in calculations of the wave velocity c/n) and k is the extinction coefficient. For single-frequency calculations, \tilde{n} is related to the dielectric constant ($e^{i\omega t}$ dependence assumed) by

$$\tilde{n}^2 = \epsilon - i \frac{\sigma}{\omega} \quad (46)$$

Conversely,

$$\epsilon = n^2 - k^2 \quad (47)$$

$$\sigma = 2nk\omega \quad (48)$$

As an example of the use of these relations, consider the dynamic bleaching of photoresist. According to the Dill model [5],

$$\tilde{n} = n - i \frac{\lambda(A \cdot M + B)}{4\pi} \quad (49)$$

where A is the bleachable absorption coefficient, B is the non-bleachable absorption, and M is the normalized photoactive compound (PAC) concentration. The dynamic behavior of the PAC is determined by

$$\frac{\partial M(\vec{r}, t)}{\partial t} = -C I(\vec{r}, t) M(\vec{r}, t) \quad (50)$$

Here C is a constant and $I(\vec{r}, t)$ is the local time-averaged intensity

$$I(\vec{r}, t) = \frac{1}{2} \Re (\vec{E} \times \vec{H}^*) = \frac{E^2(\vec{r}, t)}{2\eta_0} n$$

with $\eta_0 = 120\pi$, the free space impedance.

Figure 8 presents a flowchart of a simple algorithm for simulating the dynamic exposure process. In this procedure the total absorbed energy for the system (dose) is divided into N_d increments. The exposure for each step is simulated to a steady-state condition assuming the dielectric parameters remained fixed. The calculated intensities are then considered to be constant throughout the subdose and the parameters updated for the next increment. These simplifications to the analysis, similar to the assumptions used in SAMPLE calculations, need to be verified for accuracy. They are based upon the fact that the time scale for bleaching is several orders of magnitude larger than the time discretization of the simulation algorithm.

Assuming this piecewise-constant representation of the intensity, the PAC concentration can be calculated using

$$M(\vec{r}, t) = M(\vec{r}, 0)e^{-CI(\vec{r}, t)t} = M(\vec{r}, 0)e^{-C\mathcal{E}(\vec{r})} \quad (51)$$

where \mathcal{E} is the absorbed dose ($\sum_n I_n \cdot t_n$). The number of time steps necessary for good accuracy is clearly dependent upon the A , B , and C parameters of the resist. Contrast enhancement (CEM) resists, for example, with a large A coefficient may require over 100 dose steps while a more conventional resist only 15-20 increments.

5.3 Highly Conductive Materials

In the visible and deep-ultraviolet frequencies of interest to photolithography, the complex index of refraction of highly conductive materials can vary quite rapidly due to polarization resonances. In particular, common metals such as aluminum experience regions of anomalous dispersion within the g-line (436 nm) and deep-UV regimes which result in strong absorption with correspondingly large extinction coefficients k . As can be seen from (47), this yields a negative value for the real part of the dielectric permittivity ϵ . Although

this situation has a physical basis in the interchange between displacement and conductive current, it causes the simulation algorithm to be numerically unstable.

It is not known if this instability is inherent to the mathematics of the algorithm or if it can be attributed to the choice of discretization parameters. The stability criterion of equation (18) was derived assuming lossless dielectrics, but has been empirically shown to extend to conductive gratings outside regions of anomalous dispersion. In the latter regimes, the phase velocity is well known to exceed the speed of light [26] and this may contribute to the observed error. Reducing the time discretization to handle $v_{max} > c$, however, makes the computation less efficient and has not resolved the instability problem. The real cause of the problem may be due to strictly algorithmic considerations which have not been explored theoretically. These issues have not been addressed because previous studies using time-domain methods have assumed perfect (or weak) conductors.

One method to avoid the stability problem while retaining sufficient accuracy is to replace the anomalous situation with a nearly equivalent condition with $n \approx k$. In the former situation the absorption is extremely large resulting in almost perfect reflection. With $n \approx k$ almost unity reflection is also observed, but with a different phase shift. This method has been shown to produce excellent results for bare gratings, but the validity may break down with resonant structures (e.g. two-layer dielectric stack on an aluminum substrate).

Chapter 6

Tests and Applications

In this chapter, several test examples and applications are presented to demonstrate the accuracy and flexibility of the algorithm for a wide range of situations of interest to optical lithography. Wherever possible, rigorous simulation programs such as SAMPLE and integral equation methods are used for comparison. Several of the more complex examples involving alignment and exposure over permeable topography await experimental verification. Unless otherwise noted, all simulations assume normal incidence and TE polarization.

6.1 Layered Dielectric Media

To assess the intrinsic limits of the algorithm and the relative merits of different boundary conditions, each version of the implemented code was used to determine reflectivities from layered dielectric stacks. Table I summarizes the results for a normally incident plane wave ($\lambda = 0.4358 \mu\text{m}$ for the four cases illustrated in Figure 9. Both the first and second-order absorbing boundary conditions discussed earlier are compared.

Table I: Comparison of diffraction efficiencies for the examples of Figure 9

Case	First-Order	Second-Order	Theoretical
Perfect Conductor	0.9993 (0.07%)	0.9996 (0.04%)	1.0000
Resist	0.06266 (2.76%)	0.06412 (0.50%)	0.06444
Silicon	0.4446 (3.16%)	0.4372 (1.44%)	0.4310
Resist/Silicon	0.1510 (5.52%)	0.1422 (0.63%)	0.1431

A 256×128 ($N_y \times N_x$) grid was chosen to coincide with the maximum domain size permissible with all versions of the program with the prototype system currently available

at Berkeley. The period of the structure was set to $2.0 \mu\text{m}$, corresponding to $33.2 \text{ nodes}/\lambda$ in the resist and $11.6 \text{ nodes}/\lambda$ in the silicon. To emulate the perfectly conducting condition a conductivity of $10^{37} \Omega^{-1}$ was used. Absorbing boundary conditions were applied $0.2 \mu\text{m}$ (0.46λ) into the lowest material layer to simulate unimpeded propagation (equivalent to an infinite thickness). The first order conditions agree to within $\approx 5\%$ with theoretical calculations based upon the Fresnel relations [27], while the second-order conditions reduce the error to below 1.5% . Direct comparison of the fields indicate corresponding amplitude (as opposed to power) errors approximately one half the quoted values. As expected, the simpler conditions produce less accurate results as the conductivity of the medium increases due to the phase shift between the electric and magnetic fields. The perfectly conducting case is an exception because the fields do not penetrate to the lower boundary.

6.2 Diffraction Gratings

Symmetric

Diffraction gratings made from highly conductive materials provide an excellent test for the robustness of the absorbing boundary conditions because they are capable of scattering into many angles simultaneously and have been extensively studied using rigorous electromagnetic methods [28,29]. Table II compares results from simulations of a symmetric perfectly conducting echelle (triangular profile) grating with data obtained using well-established integral equation approaches investigated by Petit and Kalhor [30]. Figure 10 presents a schematic of the structure.

Because the first order conditions are sensitive to the specified angle of absorption, results are presented for $\theta_{abs} = 0^\circ$ and the angle of best results. For all simulations, symmetry in the calculated efficiencies was preserved to better than 0.001% . To keep the top of the grating away from the top boundary while maintaining consistency between versions, the grid size was limited to 128×128 . The data clearly highlights the inadequacy of the first

Table II: Comparison of diffraction efficiencies for the gratings of Figure 10.

		D_0	$D_1 = D_{-1}$	$D_2 = D_{-2}$	Total Energy
Slope of 0.15	Kalhor	0.699	0.147	0.004	1.000
	Petit	0.697	0.147	0.004	0.999
	First Order ($\theta = 0^\circ$)	0.688	0.132	0.003	0.959
	First Order ($\theta = 10^\circ$)	0.701	0.134	0.003	0.975
	Second Order	0.704	0.150	0.004	1.013
Slope of 0.30	Kalhor	0.182	0.357	0.051	0.999
	Petit	0.179	0.357	0.052	0.999
	First Order ($\theta = 0^\circ$)	0.228	0.277	0.029	0.839
	First Order ($\theta = 35^\circ$)	0.219	0.350	0.037	0.993
	Second Order	0.175	0.377	0.059	1.048
Slope of 1.0	Kalhor	0.472	0.099	0.163	0.995
	Petit	0.457	0.103	0.167	1.034
	First Order ($\theta = 0^\circ$)	0.368	0.151	0.072	0.811
	First Order ($\theta = 50^\circ$)	0.591	0.141	0.066	1.004
	Second Order	0.494	0.099	0.169	1.028

order conditions for the higher order modes (at angles of 25.9 and 60.88° off the normal), particularly at the larger slopes. On the other hand, the second order relations produced reasonable agreement at all slopes with conservation of energy to within 5%. Further improvements on these results may be possible by reducing grid step size h , increasing the number of iterations, and optimizing the matching of the analytic and numerically computed incident fields.

Typical execution times for the above examples (≈ 1000 time steps, VP Ratio = 16) were 20 seconds for the first order conditions and 30 seconds for the second order conditions. For a fully configured system with at least 16K processors, these values would be reduced to roughly 2 and 3 seconds, respectively.

Asymmetric

The two echelle gratings illustrated in Figure 11 were used to investigate the sensitivity of the absorbing conditions to asymmetries in topography. Table III presents results of the

simulations for a 256×128 grid along with results from the integral equation program of Kalhor for comparison.

Table III: Comparison of diffraction efficiencies for the asymmetric gratings of Figure 11.

		D_0	D_1	D_{-1}	D_2	D_{-2}	Total Energy
Slope = 5°	Kalhor	0.7611	0.0857	0.1392	0.0131	0.0056	1.0048
	First Order ($\theta = 0^\circ$)	0.7933	0.0743	0.1043	0.0013	0.0006	0.9738
	First Order ($\theta = 10^\circ$)	0.7972	0.0754	0.1064	0.0014	0.0006	0.9811
	Second Order	0.7555	0.0906	0.1488	0.0103	0.0043	1.0090
Slope = 13.8°	Kalhor	0.0511	0.1440	0.7357	0.0585	0.0011	0.9904
	First Order ($\theta = 0^\circ$)	0.0482	0.1581	0.6568	0.0069	0.0004	0.8704
	First Order ($\theta = 28^\circ$)	0.0515	0.1725	0.7983	0.0085	0.0001	1.0310
	Second Order	0.0507	0.1481	0.7911	0.0484	0.0005	1.0388

For these structures, the first and second orders correspond to waves striking the top surface at angles of 28.4° , and 72.2° , respectively, with respect to the normal. As before, the second order conditions provide far superior absorption of the higher order modes.

Grid Size Effects

To separate the effects of the discretization from the errors introduced by the absorbing boundary conditions, each of the above gratings was tested with a wide range of mesh sizes. The results for the second order relations are summarized in Table IV. Only the deepest gratings are represented to illustrate the trends. Execution times include all overhead for time stepping and testing for steady-state behavior on the 1K machine at Berkeley.

Table IV: Comparison of D_m for various grid sizes

	Grid Size	D_0	D_1	D_{-1}	D_2	D_{-2}	# Iter.	Time (sec)
Symmetric, slope of 0.3	64 × 64	0.1844	0.3716	0.3716	0.0566	0.0566	822	16.3
	64 × 128	0.1732	0.3751	0.3751	0.0580	0.0580	822	16.0
	128 × 128	0.1728	0.3817	0.3817	0.0571	0.0571	942	27.7
	256 × 256	0.1754	0.3792	0.3792	0.0551	0.0551	1342	140.8
	Integral	0.1820	0.3571	0.3571	0.0511	0.0511	—	—
Symmetric, slope of 1.0	32 × 32	0.4987	0.1040	0.1040	0.1548	0.1548	822	—
	64 × 64	0.4967	0.0960	0.0960	0.1714	0.1714	822	16.3
	64 × 128	0.4901	0.1024	0.1024	0.1488	0.1488	822	15.9
	128 × 128	0.4937	0.0959	0.0959	0.1681	0.1681	942	27.7
	256 × 256	0.5042	0.0994	0.0994	0.1873	0.1873	1342	141.1
	Integral	0.4720	0.0990	0.0990	0.1625	0.1625	—	—
Asymmetric, slope of 13.8°	64 × 64	0.0425	0.1374	0.7972	0.0567	0.0024	834	16.1
	64 × 128	0.0369	0.1331	0.8276	0.0321	0.0012	834	16.1
	128 × 64	0.0500	0.1505	0.7892	0.0491	0.0006	942	18.2
	128 × 128	0.0490	0.1532	0.7842	0.0419	0.0010	966	28.3
	256 × 128	0.0507	0.1481	0.7911	0.0484	0.0005	1054	57.0
	128 × 256	0.0434	0.1617	0.7904	0.0644	0.0003	1054	57.1
	256 × 256	0.0532	0.1555	0.7800	0.0315	0.0007	1182	124.2
	Integral	0.0511	0.1440	0.7357	0.0583	0.0011	—	—

The number of grid points in the horizontal direction (N_y) determines the density of the mesh ($h = N_y/d$) while the number in the vertical dimension (N_x) specifies the height of the top boundary and hence the proximity of the grating surface to the absorbing boundary conditions. One would expect that the higher profile grids ($N_x > N_y$) would yield better results for a fixed N_y for two reasons: the absorbing boundaries are further removed from edges and the fields along line CD better represent the far field behavior. No clear pattern can be observed from the data, however, suggesting that other factors are more prominent.

The density of the grid is one such parameter. As the spatial step size h is reduced, the accuracy of the results improves. This is due partly to the accompanying reduction of the time discretization dt , equation (18), and partly to the finer representation of the grating surface. The improvement for these cases is modest because even the coarsest grid (32×32 with $14 \text{ pts}/\lambda_0$) is finer than the nominal $10 \text{ pts}/\lambda$ rule of thumb. These considerations indicate that the primary errors can be attributed to inherent characteristics of the algorithm and imperfect modeling of the absorbing conditions. The results for the perfectly conducting plane in the previous subsection (0.04% power discrepancy) favor the latter explanation.

6.3 Dynamic Exposure on Flat Substrates

As a final test, the dynamic capabilities of the algorithm were tested by simulating exposures on flat substrates which could be accurately verified using SAMPLE. Figure 12 shows the structure used for these examples. Due to standing waves in the photoresist, the reflectivity of the unexposed stack is a maximum (minimum) when the resist thickness is an even (odd) multiple of $(\lambda_{resist}/4)$. At these extremes the power coupling into the resist is a weak function of thickness variations. In between, at half-integral quarter wavelengths, the coupling is strongly dependent upon film thickness.

Figures 13 and 14 illustrate results obtained for resist thicknesses of 5.5 and $6.0 \lambda/4$.

respectively. The grid dimensions were 128×128 . In both cases the reflectivities match the SAMPLE simulations extremely well. These results are somewhat atypical in that the discretization of the resist required an integer number of grid points. When the thickness was chosen to fall in between two grid points, the observed error in the reflectivities was up to 5% larger although the general shape of the bleaching curve was preserved. Reductions in the grid size could improve the accuracy at the expense of greater memory and longer run times. The problem is rooted in the uniform grid assumption of the method, however, and conversion to a finite element approach is the best solution.

For exposure, the main quantity of interest (and the best measure of the success of the simulation) is the spatial distribution of the inhibitor concentration. Figure 15 presents results for a $0.405 \mu\text{m}$ resist thickness following $50 \text{ mJ}/\text{cm}^2$ with a normally incident plane wave. The resist ABC parameters were $A = 0.54 /\mu\text{m}$, $B = 0.06 /\mu\text{m}$, and $C = 0.014 \text{ cm}^2/\text{mJ}$. The two curves overlap very well throughout the entire thickness, verifying the accuracy of the time domain solution. The small discrepancies near the extremes are due to different placements of the 50 node points within the resist by SAMPLE.

6.4 Asymmetry Effects in Alignment

It is well known that asymmetry in underlying topography and resist coatings from typical process variations can amplify uncertainties in alignment [6]. The aim of this section is to illustrate the flexibility of the time domain method to investigate the physical mechanisms.

Figure 16 depicts an alignment structure consisting of a recessed mark in silicon coated with photoresist, similar to the targets examined in reference [6]. To distinguish scattering from the resist surface and substrate, the first-order efficiencies for diffraction from each profile (treated independently as homogeneous surfaces) are plotted in Figures 18 and 19 as a function of the angle of asymmetry. The models for the two cases are shown in Figure 17. The first orders were chosen because of their importance in dark field alignment systems.

As expected, the greater reflectivity of silicon increases the sensitivity to the asymmetry. As the slope of the right edge is reduced, the -1 mode contribution increases at the expense of the +1 order causing a shift in the apparent location of the edge.

To examine the relative effects of asymmetry in each feature in the combined structure, simulations on an identical mark with a $1.0 \mu\text{m}$ lossless resist ($\bar{n} = 1.68$) were performed. Figure 20 illustrates the changes in the far-field image calculated using (41) for substrate asymmetries of -5° , 10° , and 20° . A normally incident plane wave with $\lambda = 0.488 \mu\text{m}$ illuminated the mark. Note that the scales for mark are distorted such that the groove appears much shallower than it really is. For this choice of parameters, decreasing the steepness of the silicon edge caused the central peak to rise and shift to the side of the asymmetry. The apparent location of the other edge was not strongly affected.

Figure 21 depicts the results when the slope of the resist profile on one side is varied by -4° and 4° . As before, the edge with the asymmetry was most sensitive to the asymmetry. The magnitude of the changes are larger than in the substrate case above, presumably because the slope asymmetry in the resist extends over a greater fraction of the period. These conclusions need to be examined more thoroughly in a controlled study of the effects of both parameters and tested experimentally. Nevertheless, the results illustrate the importance of resist coating uniformity in alignment and the usefulness of the method for isolating the various factors.

When the thickness of the resist coating is reduced, the upper surface in the groove may drop below the edges of the mark as illustrated in Figure 22. This interpenetration cannot be simulated using the approximate Rayleigh expansion method outlined in [6,7]. Figure 23 depicts the corresponding image. The effects of the resist for this fairly conformal coating appear to be weaker and the image more representative of the underlying profile.

6.5 Diffraction from Latent Images

Diffraction from latent images formed during exposure has been suggested as a technique for in-situ focus and/or exposure monitoring [31]. A complete quantitative analysis of the potential sensitivity of the method requires consideration of off-axis incident rays. Nevertheless, insight into the viability of the process can be obtained with a simple normal incidence model. Figure 25 shows the simulated first order (with respect to $\theta_{inc} = 0^\circ$) diffraction efficiencies for a $0.75 \mu\text{m}$ periodic equal line-space pattern in AZ-type photoresist as a function of exposure dose. Bleaching of the resist was calculated using the Dill formulation discussed in Section 5.2 with $n = 1.68$. The efficiencies are normalized with respect to clear field (uniform unity-amplitude illumination). The incident image and topography profiles are illustrated in Figure 24. Table V lists the parameters used by SAMPLE to calculate the aerial exposure image. For simplicity, the measurement wavelength is assumed to coincide with exposure signal. As the resist bleaches, the latent image scatters more power into the higher order harmonics resulting in a monotonic increase with exposure (possibly focus dependent). For this particular situation, the efficiencies are quite small but follow a smooth linear pattern.

Several considerations need to be kept in mind when interpreting these results:

- To convert the SAMPLE images to incident fields for the top boundary. E_z is set to $\sqrt{2\eta I(y)} \sin(\omega t)$. In effect, this assumes that the field is *at focus* along C-D because the distribution corresponds to an amplitude-modulated plane wave. The actual field, however, is given by a plane wave expansion such as (35) from diffraction off the mask where the time dependence is tied to the spatial dependences and quadrature terms are present. A more exact representation of the field would require knowledge of the NA of the imaging lens and pattern period d (to determine the maximum number of harmonics) and would involve solution of a nonlinear set of equations to match the

Table V: Simulation parameters for latent image exposure.

Wavelength	0.4358 μm
Numerical aperture of exposure optics*	0.28
Coherence factor of illumination*	0.7
Defocus*	1.39 μm
Exposure intensity	100 mW/cm ²
Mask pattern*	0.75/0.75 μm linespace
ABC coefficients of photoresist	A = 0.551 / μm B = 0.058 / μm C = 0.01 cm ² /mJ
Real part of photoresist refractive index	1.68
Refractive index of substrate	4.73 - i 0.136
Resist thickness	0.4358 μm
Exposure dose	50 mJ/cm ²

* parameters used only by SAMPLE for calculation of the aerial image

time-averaged local field to the SAMPLE image using orthogonality. Even then the result is approximate because partial coherence effects have been neglected.

- Since the incident signal is a sum of plane waves, each component wave requires a distinct periodic phase shift ϕ . This poses a problem because the fields are treated as a composite signal and the various components are unknown. If the numerical aperture of the mask illumination lens is small (almost spatially coherent), however, then Floquet's theorem indicates that, to a good approximation, the fields incident at the wafer are *instantaneously* equal at increments of the period d . In this case, the $\theta_{inc} = 0^\circ$ boundary conditions may produce good results.
- Once the incident (assumed in focus) profile is specified, the algorithm updates and propagates the magnetic fields self-consistently using (16) and (17). As a result, the fields begin to diffract before they reach the surface of the topography. Lower numerical aperture imaging lenses have a larger depth of focus ($\lambda/2NA^2$) and thus introduce smaller errors in the focus approximation.

For the case considered above, the NA of the illumination and imaging lenses are both small, 0.2 and 0.28 respectively, so the periodicity and focus simplifications should be valid. Experimental corroboration will be necessary to test the accuracy of these approximations.

6.6 Exposure in Contrast Enhancement Materials

The need for improved contrast in lithography has paced the development of advanced resist technologies such as contrast enhanced materials (CEM). In the CEM process a layer with high but bleachable absorption is deposited over a standard resist. The exposed regions become highly transparent while the low intensity areas remain highly absorbing, producing a well-defined exposure window for the underlying resist which can improve pattern resolution. At the same time, however, the CEM layer can act like a second mask and cause interesting diffraction effects within the resist. Mack et al. [32] investigated this phenomenon using a Kirchhoff diffraction approach for near fields and concluded that normal, inverted, and hourglass line patterns can be formed depending upon the numerical aperture of the imaging lens and the CEM resist parameters and development characteristics.

To examine these issues, the algorithm was applied to simulate exposure in a typical CEM process which is illustrated in Figure 26. The dimensions of the printed feature ($0.48 \lambda/NA$) are representative of the current resolution limit for CEM materials [33]. Table VI presents the conditions used by SAMPLE for the aerial calculation. The considerations outlined in the previous section also apply here. Figure 27 plots contours of the inhibitor concentration following a 350 mJ/cm^2 exposure. For the given set of parameters, we see some two-dimensional spreading of the intensity near the edges of the CEM aperture as witnessed by the extension of the outer contours further into the masked regions. The slight inward bow near the substrate and in the center of the window where diffraction effects should be less prominent are probably due to attenuation as the signal propagates through the resist.

Figure 28 depicts the simulated profile after an 80 second development using the SAMPLE development module with resist parameters of $E_1 = 5.63$, $E_2 = 7.43$, and $E_3 = -12.6$. The corresponding image from the SAMPLE CEM exposure facility is shown for comparison. Although the scales are slightly different, the two profiles bear a striking resemblance, especially with regard to the undercut of the standing waves at the bottom of the resist. Slight differences can be observed in the standing wave ratios throughout the resist where the two-dimensional simulation indicates more pronounced variations deeper in the resist. The uniformity suggested by SAMPLE could be due to the neglect of two-dimensional effects or to discretization errors arising from SAMPLE's use of only 50 horizontal layers versus 256 for the time domain situation. From these results, then, the extent of two-dimensional diffraction is difficult to ascertain, but appears not to be very strong.

Table VI: Simulation parameters for contrast enhancement material (CEM) exposure.

Wavelength	0.4358 μm
Numerical aperture of exposure optics*	0.28
Coherence factor of illumination*	0.7
Defocus*	1.39 μm
Exposure intensity	100 mW/cm ²
Mask pattern*	0.75/0.75 μm line/space
ABC coefficients of CEM	A = 12.0 / μm B = 0.0001 / μm C = 0.064 cm ² /mJ
ABC coefficients of photoresist	A = 0.551 / μm B = 0.058 / μm C = 0.01 cm ² /mJ
Refractive index of CEM and photoresist	1.68
Refractive index of oxide	1.47
Refractive index of substrate	4.73 - i 0.136
CEM thickness	0.4000 μm
Resist thickness	0.7133 μm
Thickness of underlying oxide	0.0741 μm
Exposure dose	50 mJ/cm ²

* parameters used only by SAMPLE for calculation of the aerial image

6.7 Reflective Notching

An important example of the role of two-dimensional topography effects in lithographic processes is reflection from steps or notches in the substrate. Exposure in the vicinity of highly conductive materials such as aluminum lines can produce unexpected variations in the linewidth of adjacent features due to propagation of the reflected signal through the resist. Matsuzawa et al. [13] simulated these effects for a stepped reflective substrate using a hybrid finite element/boundary element method. Their model, however, only applies for perfectly conducting substrates and is computationally intensive. For example, simulations of exposure to a dose of 50 mJ/cm^2 consumed over 24 minutes of CPU time on an HITAC S-810 vector processing supercomputer operating at 630 MFLOPs.

Figure 29 depicts the structure used by Matsuzawa et al. To facilitate comparison of the accuracy and efficiency of the time-domain approach with the finite element technique, identical simulation parameters were used (Table VII). Because the exact resist profile was not specified, the surface was modeled with a slope of -2° out to $2.0 \mu\text{m}$ tapering to -1° out to $4.0 \mu\text{m}$. In the above report, the simulation boundary was stopped at $2.5 \mu\text{m}$ to reduce the required memory and computation time. Because one of the important goals of this study is to examine asymmetries caused by the topography, however, the domain was extended out beyond the mask edge for the calculations.

Figures 30 and 31 show the photosensitizer contours and developed profiles, respectively, obtained using both methods. Our analysis used a 256×256 grid and separated the exposure into 15 dose steps. The SAMPLE development routines were modified to account for the steps in the topography. The two profiles predict similar qualitative behavior. The interaction of the incident signal with the step produces a characteristic cusp is near the step-substrate corner and a larger sidewall slope due to deflection off the notch. As a result, the edges of the feature on the side with the step are sharper than expected for an isolated line.

Table VII: Simulation parameters for reflective notching.

Wavelength	0.365 μm
Numerical aperture of exposure optics*	0.42
Coherence factor of illumination*	0.5
Defocus*	1.35 μm
Exposure intensity	100 mW/cm ²
Mask pattern*	Isolated 2.0 μm line
ABC coefficients of photoresist	A = 0.74 / μm B = 0.20 / μm C = 0.012 cm ² /mJ
Refractive index of photoresist	1.68
Resist thickness	0.8 μm (nominal)
Exposure dose	50 mJ/cm ²

* parameters used only by SAMPLE for calculation of the aerial image

To match the two profiles, our simulations required a development time of 80 seconds compared to the 40 seconds cited in [13]. The discrepancy may be due to errors in modeling the resist thickness or errors in the quoted development parameters. It is well known that variations of $\lambda/4 = 0.054\mu\text{m}$ can produce up to 50% changes in the local exposure (for flat substrates). Nevertheless, comparison with the actual photoresist image illustrated in the Figure 32 shows good qualitative resemblance, supporting the validity of the two-dimensional approach. Improvements in the accuracy of the results might be achieved by reducing the simulation domain to 2.0 μm . Unless the resist thickness is known more accurately, however, the degree of quantitative correspondence and the limitations of the simulation remain unclear.

The time-domain approach offers an order of magnitude (or better) speed advantage over the method of Matsuzawa et al., primarily due to the efficiency and parallelism of the formulation. Simple calculations indicate a reduction of the CPU time by a factor of ~ 4 from 15.4 GFlop-min to 3.9 GFlop-min for the case examined above (63 minutes on the Berkeley system with 256×128 grid). Several factors, chosen conservatively for the simulation, could improve on this value by at least a factor of two. First, experience with

the SAMPLE program and the above results suggests that the number of dose steps could probably be reduced from 15 to approximately 10. Second, an extra savings of up to 40-50% might be achieved by using the fields at the end of the previous dose simulation as a starting point for calculations at the next interval. This simplification assumes that the extent of bleaching between time steps is small enough that the previous solution is approximately correct with the updated parameters. Third, this example pushed the limits of the prototype system at Berkeley and appeared to suffer from both memory and communication bottlenecks. A commercial Connection Machine system (available in 16K or larger configurations) would alleviate some of these problems, particularly the memory limitations. This would allow the code to be optimized by removing restrictions upon the allocation of variables which compromised the efficiency of the implementation of the costly boundary conditions. It should be kept in mind that periodic version of the algorithm (used in the CEM and latent image exposures) executes about 20-30% more efficiently than the version for isolated structures because of the simpler boundary conditions on the sides.

Chapter 7

Extensions and Future Work

The implementation of the algorithm examined in Chapter 6 is suitable for simulation of arbitrary periodic or isolated structures with normally incident TE-polarized illumination. In order to investigate focus and latent image diffraction issues more thoroughly, the periodic boundary conditions for arbitrary incident angles (Section 4.2) need to be debugged. Extensive experience with testing the algorithm suggests that the conditions should be *stable* for incident angles up to 5 or 10° and possibly for the full range (90°). The limits for stability and accuracy will play an important role in the application of the algorithm. For isolated structures, of course, phase conditions are not necessary and arbitrary angles of incidence pose no problem provided the values of the incident field are carefully accounted for. In this case, the corresponding equation to (29) becomes very complex and memory intensive while the interpretation of the incident and scattered fields more subtle. To prevent mistakes in programming, the incident field for this situation would follow the more common electromagnetic definition: the wave which would propagate *in the absence of the scatterer*; that is, the substrate and topography. This is the convention used for the top boundary in contrast to the modified interpretation applied on the side boundaries which is discussed at the end of Section 4.2. The scattered field is the remaining field which takes attenuation and diffraction into consideration.

Improvement of the accuracy of the algorithm for general topography can be achieved by development in two key areas. First, schemes for reducing reflections from absorbing boundary conditions should be explored. Methods such as the Superabsorption technique introduced by Mei et al. [24], which relies upon cancellation of leading order errors through multiple application of the boundary operators, may enhance the robustness of the condi-

tions for fields at grazing incidence. Second, conversion to a finite element formulation in the time domain would reduce discretization errors due to material boundaries which fall between nodes. This effect becomes especially critical for situations in which resonances can be excited. The finite difference method can be adapted to a nonuniform grid by locally modifying the spatial increment (h), but sloped features still present a problem which is properly addressed by the finite element approach. One potential disadvantage of the finite element formulation, which needs to be examined more closely, is the difficulty to map the domain to a regular grid format to exploit the parallelism of the Connection Machine. Note that if a nonuniform grid is established for only one (or two for a three-dimensional domain) dimension, only minor modifications are necessary for the finite difference approach.

Longer term issues for the algorithm primarily concern interfacing the program to fill a critically missing link in an integrated optical lithography CAD system. Simulation programs such as SAMPLE and SPLAT [34] are available to model propagation and scattering of optical signals through elements such as masks, optics, and aperture stops. The Fourier diffraction approach used by these simulation tools, however, does not apply to scattering from "thick" features such as wafer topography. The role of the rigorous time domain program would thus be to propagate the aerial image calculated by these simulators to the wafer and back to a plane for further analysis through the collection optics. The various stages in this process can be clearly identified in the unfolded representation of the optical system illustrated in Figure 33. By combining existing simulation tools in this manner, alignment, exposure, and overlay over complex nonplanar topography could be modeled. When further linked with rigorous development and etching routines, a complete environment suitable for simulation of three-dimensional integration processes might be envisioned.

Before this gap can be filled, the issue of partial coherence in the illumination system needs to be addressed. In commercial lithography systems, the numerical aperture of the illumination lenses is usually restricted such that a degree of spatial coherence between fields

originating from different points in the source is achieved on the mask. As a result, mutual interactions between these fields affect their propagation through the optics and ultimately their diffraction from the topography. The Hopkins theory of diffraction adopted in SPLAT and SAMPLE accounts for these interactions in a neat, analytic framework which has been experimentally verified. Much work remains to be done, however, to determine an accurate and effective way of modeling the effects of partial coherence in topography scattering.

The most tedious, but physically insightful, method would be to divide the source into segments and trace the fields from each segment through the optical system, off the wafer, and back. A more efficient approach might be possible by modeling the interactions as biased, quasi-random phase shifts between fields at adjacent points in space [35]. This could be implemented on the Connection Machine by allocating extra processors along the incident field boundaries to introduce appropriate phase shifts in the time domain representation of the incident field. The exact form and determination of these phase shifts remains to be delineated.

Finally, we should note a few observations concerning the limitations of the Connection Machine organization encountered during this study and how these might be impacted by future developments. The machine is still somewhat of an experimental system and new features are constantly being introduced to suit the needs of users. For this algorithm, communications play an important, if not more important, role than floating point operations. Streamlining local communication channels might reduce algorithm overhead by up to 30-50% from the current ~ 3 Flops/communication penalty. Another constraint, briefly discussed earlier, is the 64K bit local memory limitation. The large domains and fine meshes required for finite difference/element formulations strains the local stack capabilities and requires variable-saving simplifications to be made which limit efficiency. As an illustration, the absorbing boundary conditions on the side require knowledge of the incident field. So that larger domains could be accommodated, these operations were performed in the dummy

layers and then stored in the boundary nodes. This could be accomplished more efficiently if the calculations were performed globally and sent during normal communications, possible only if local memory were increased.

Chapter 8

Conclusion

A rigorous new time domain method for simulation of topography scattering issues in optical lithography has been developed and verified for accuracy. The approach is very similar to finite difference techniques used for electromagnetic scattering analysis, but has been reformulated to exploit the parallel nature of wave propagation and the computational power of recent massively parallel architectures such as the Connection Machine. Efficient new absorbing boundary conditions were devised to reduce the time spent updating boundary nodes and existing conditions were modified to account for lossy dielectrics. To address the special needs of optical lithography applications, new periodic boundary conditions were added along with rapid techniques for obtaining frequency-domain information such as diffraction efficiencies.

The resulting code, implemented on a Connection Machine CM-2, has been applied to study several important two-dimensional interaction effects with a flexibility not possible with any other available technique: exposure over nonplanar topography such as reflective steps, bleaching of contrast enhancement materials, and diffraction from latent images in photoresist. At the same time, however, the parallelism of the method attained remarkable efficiency. Steady-state calculations on structures up to 8λ square required less than 40 seconds on a 1K machine, extrapolating down to a few seconds on a fully configured 16K system. These preliminary results highlight the tremendous potential of the method to explore general electromagnetic interactions in alignment, overlay, and exposure which play an increasingly critical role as integrated circuit technology pushes inherent diffraction limits.

References

- [1] W. G. Oldham, S. N. Nandgaonkar, A. R. Neureuther, and M. M. O'Toole. A general simulator for VLSI lithography and etching processes; Part I — Applications to projection lithography. *IEEE Trans. Electron Devices*, ED-26(4):14–16, April 1979.
- [2] C. A. Mack. PROLITH: a comprehensive optical lithography model. In *Optical Microlithography IV*, pages 207–220, Proc. SPIE Vol. 538, 1985.
- [3] K. S. Yee. Numerical solution of initial boundary value problems involving Maxwell's equations in isotropic media. *IEEE Trans. Antennas Propagat.*, AP-14:302–307, May 1966.
- [4] W. D. Hillis. *The Connection Machine. ACM Distinguished Dissertations*. MIT Press. Cambridge, MA, 1985.
- [5] F. H. Dill, A. R. Neureuther, J. A. Tuttle, and E. J. Walker. Modeling projection printing of positive resists. *IEEE Trans. Electron Dev.*, ED-22(7):456–464, July 1975.
- [6] N. Bobroff and A. Rosenbluth. Alignment errors from resist coat topography. *J. Vac. Sci. Technol. B*, 6(1):403–408, Jan/Feb. 1988.
- [7] G. Gallatin, J. Webster, E. Kinter, and F. Wu. Modeling the images of alignment marks under photoresist. In *Optical Microlithography VI*, pages 193–201, Proc. SPIE Vol. 772, 1987.
- [8] C. P. Kirk. Theoretical models for the optical alignment of wafer steppers. In *Optical Microlithography VI*, pages 134–141, Proc. SPIE Vol. 772, 1987.
- [9] D. Nyssonen and C. P. Kirk. Optical microscope imaging of lines patterned in thick layers with variable edge geometry: Theory. *J. Opt. Soc. Am.*, 5(8):1270–1280, Aug. 1988.

- [10] C. M. Yuan, J. Shaw, and W. Hopewell. Modeling of optical alignment images for semiconductor structures. In *Optical/Laser Microlithography VII*, Proc. SPIE. 1989.
- [11] C. B. Burkhardt. Diffraction of a plane wave at a sinusoidally stratified dielectric grating. *J. Opt. Soc. Am.*, 56(11):1502-1509, 1966.
- [12] F. G. Kaspar. Diffraction by thick, periodically stratified gratings with complex dielectric constant. *J. Opt. Soc. Am.*, 67(10):37-45, 1973.
- [13] T. Matsuzawa, A. Moniwa, N. Hasegawa, and H. Sunami. Two-dimensional simulation of photolithography on reflective stepped substrate. *IEEE Trans. CAD*, CAD-6(3):446-451, May 1987.
- [14] G. Wojcik, D. Vaughn, and L. Galbraith. Calculation of light scatter from structures on silicon surfaces. In *Lasers in Microlithography*, pages 21-31, Proc. SPIE Vol. 774. 1987.
- [15] *Connection Machine Model CM-2 Technical Summary*. Thinking Machines Corporation, April 1987.
- [16] K. Umashankar and A. Taflove. A novel method to analyze electromagnetic scattering of complex objects. *IEEE Trans. Electomag. Compat.*, EMC-24(4):397-405, Nov. 1982.
- [17] A. C. Cangellaris. *Time-Domain Computation of Electromagnetic Wave Scattering by the Method of Conforming Boundary Elements*. PhD thesis, Univ. California. Berkeley. 1985.
- [18] A. C. Cangellaris, C. C. Lin, and K. K. Mei. Point-matched finite element methods for electromagnetic radiation and scattering. *IEEE Trans. Antennas Propagat.* AP-35(10):1160-1173, Oct. 1987.

- [19] A. Taflove and M. E. Browdin. Numerical solution of steady-state electromagnetic scattering problems using the time-dependent Maxwell's equations. *IEEE Trans. Microwave Theory Tech.*, MTT-23(8):623-630, Aug. 1975.
- [20] G. Mur. Absorbing boundary conditions for the finite difference approximation of the time-domain electromagnetic-field equations. *IEEE Trans. Electromag. Compat.*, EMC-23(4):377-382, Nov. 1981.
- [21] B. Engquist and A. Majda. Absorbing boundary conditions for the wave equation. *Math. Comp.*, 31:629-651, July 1977.
- [22] R. L. Higdon. Numerical absorbing boundary conditions for the wave equation. *Math. Comp.*, 49(179):65-90, July 1987.
- [23] J. Blaschak and G. A. Kriegsmann. A comparative study of absorbing boundary conditions. *J. Comp. Phys.*, 77:109-139, 1988.
- [24] K. K. Mei and J. Fang. Superabsorption: A method to improve local boundary conditions. Submitted for publication in *J. Comp. Phys.*
- [25] X. Zhang and K. K. Mei. Time-domain finite difference approach for the calculation of the frequency-dependent characteristics of microstrip discontinuities. Submitted for publication in *IEEE Trans. Microwave Theory Tech.*
- [26] J. D. Jackson. *Classical Electrodynamics*, page 302. Wiley, second edition, 1975.
- [27] M. Born and E. Wolf. *Principles of Optics*, pages 61-63. Pergamon, sixth edition. 1980.
- [28] D. Maystre. Rigorous vector theories of diffraction gratings. In E. Wolf, editor. *Progress in Optics XXI*, chapter I, Elsevier, 1984.
- [29] T. K. Gaylord and M. G. Moharam. Analysis and applications of optical diffraction by gratings. *Proc. IEEE*, 73(5):894-937, May 1985.

- [30] H. A. Kalhor and A. R. Neureuther. Numerical method for the analysis of diffraction gratings. *J. Opt. Soc. Am.*, 61(1):43–48, Jan. 1971.
- [31] K. W. Edmark and C. P. Ausschnitt. Stepper overlay using alignment to a latent image. In *Optical Microlithography IV*, pages 91–101, Proc. SPIE Vol. 538, 1985.
- [32] T. Brown and C. A. Mack. Comparison of modeling and experimental results in contrast enhancement lithography. In *Advances in Resist Technology and Processing V*, pages 390–403, Proc. SPIE Vol. 920, 1988.
- [33] R. A. Ferguson, P. R. West, and A. R. Neureuther. Optimization of contrast enhanced lithography. presented at *KTI Microelectronics Seminar*, 1987.
- [34] K. K. H. Toh. *Two-Dimensional Images with Effects of Lens Aberrations in Optical Lithography*. Master's thesis, Univ. California, Berkeley, May 1988.
- [35] A. R. Neureuther, personal communication.

FIGURES



Figure 1: [Illegible text]

(a)

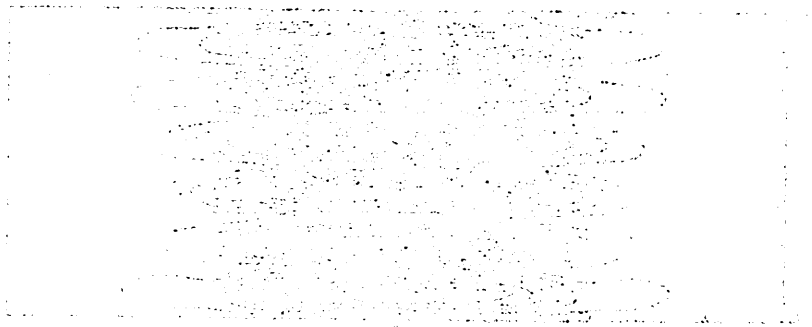
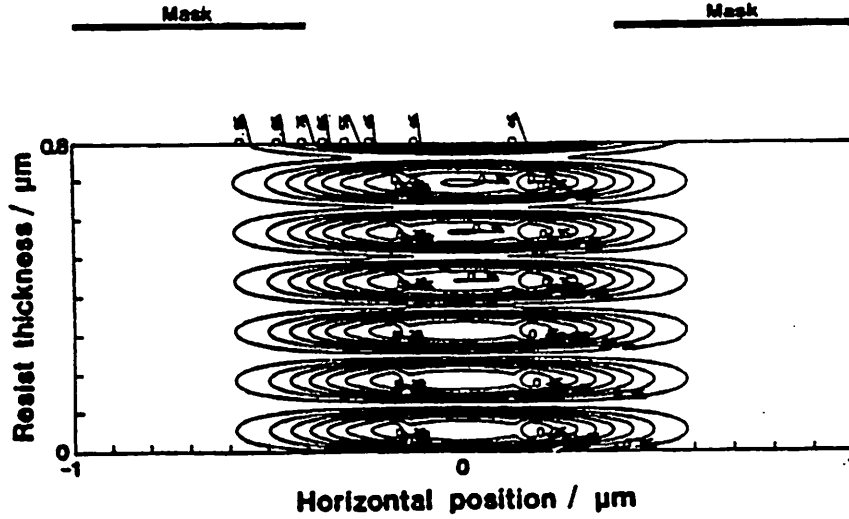


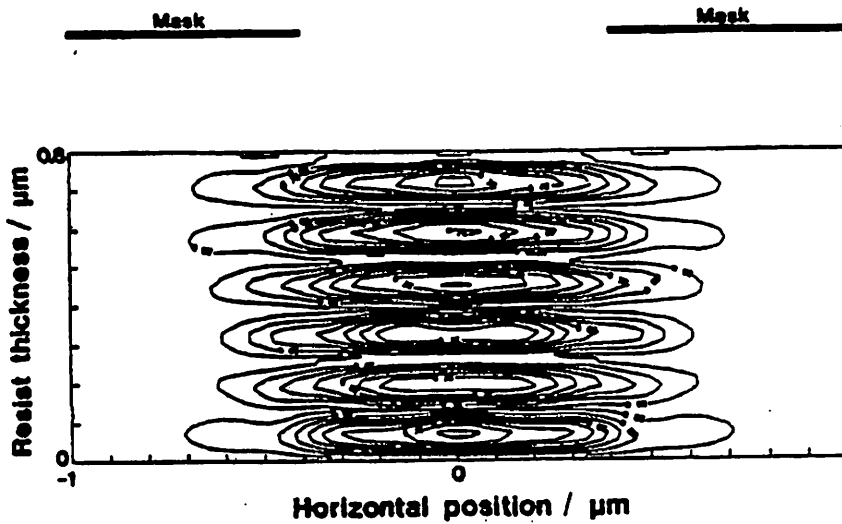
Figure 2: [Illegible text]

(b)

The following text is extremely faint and illegible. It appears to be a paragraph of text located below the figures.



(a)



(b)

Figure 1: Simulation of two-dimensional diffraction effects on a flat substrate following 50 mJ/cm^2 exposure. Normalized photosensitizer concentration contours for a $0.8 \mu\text{m}$ isolated space illuminated at $\lambda = 0.436 \mu\text{m}$ with AZ-type resist are shown. (a) Distribution on an aluminum surface as calculated by SAMPLE. (b) Distribution on a perfectly conducting surface calculated using the hybrid finite-element/boundary-element method of reference [13]).

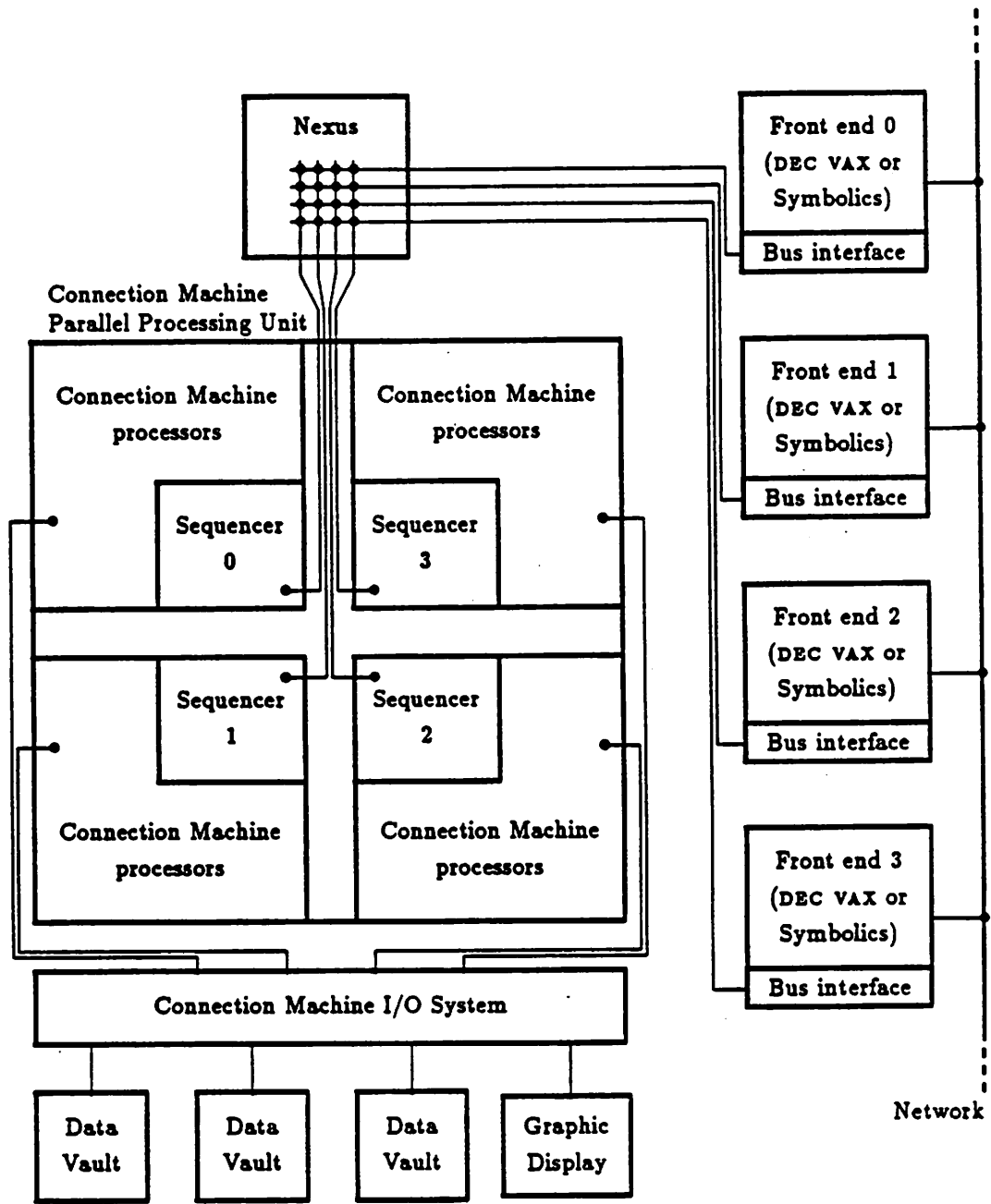


Figure 2: Connection Machine Model CM-2 system organization (From reference [15]).

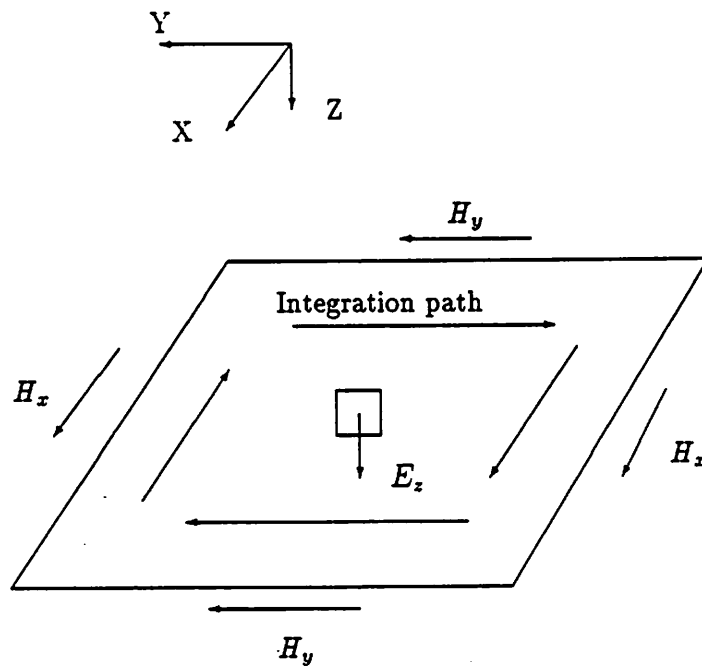


Figure 5: Integration path for equation (6).

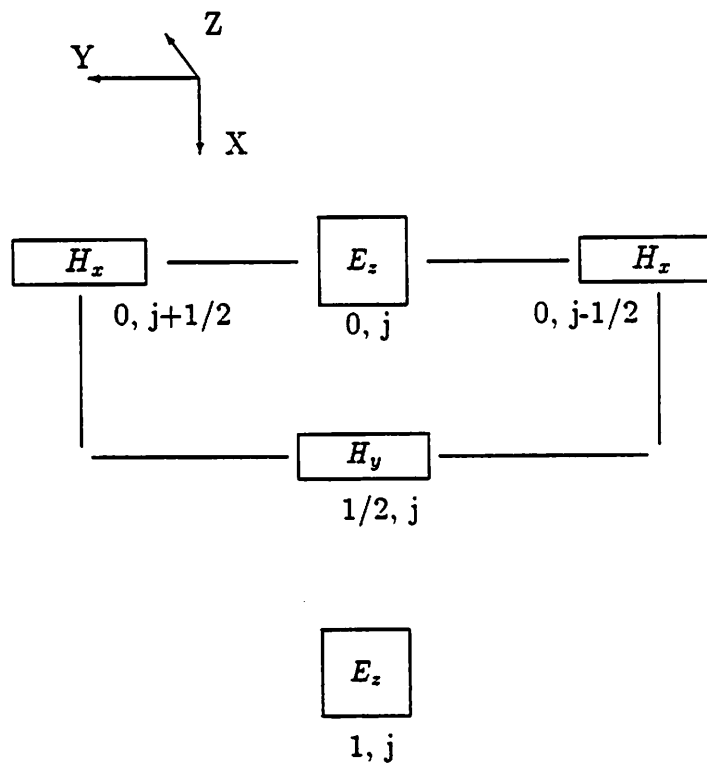


Figure 6: Boundary conditions along the boundary $x = 0$ (side C-D).

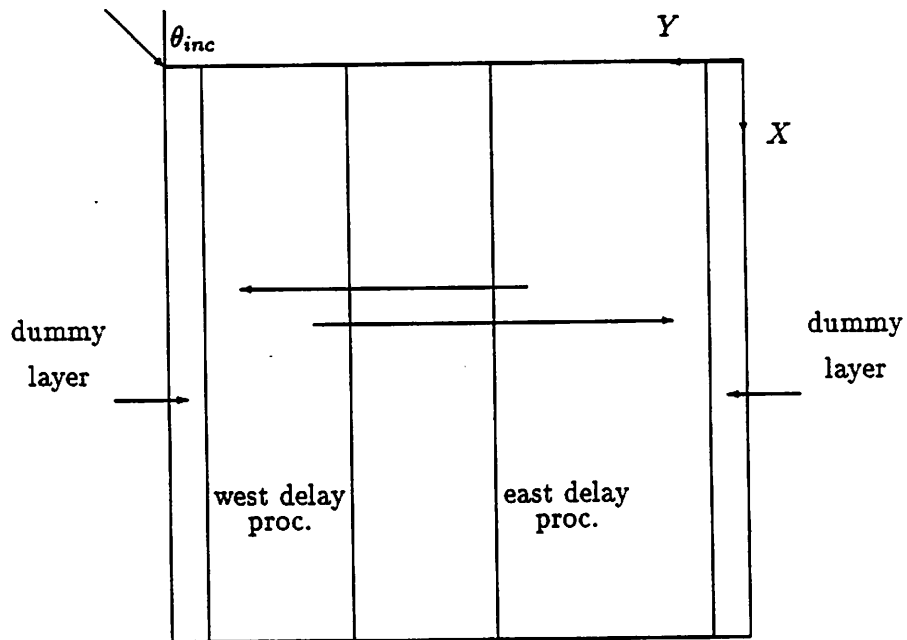


Figure 7: Illustration of delay structure for arbitrary incidence. The outermost layer of processors (*dummy layers*) calculate the incident fields for the boundary conditions. An extra variable is allocated to each processor for shifting fields along horizontal delay lines formed by two sets of nodes (east/west) as shown. At each time step the processors in each bank shift their stored value to their neighbor except for those along the innermost edge which store it directly in the boundary node on the opposite side of the domain. The number of processors in each bank is determined by the angle of incidence through an equivalent steady-state Floquet time delay.

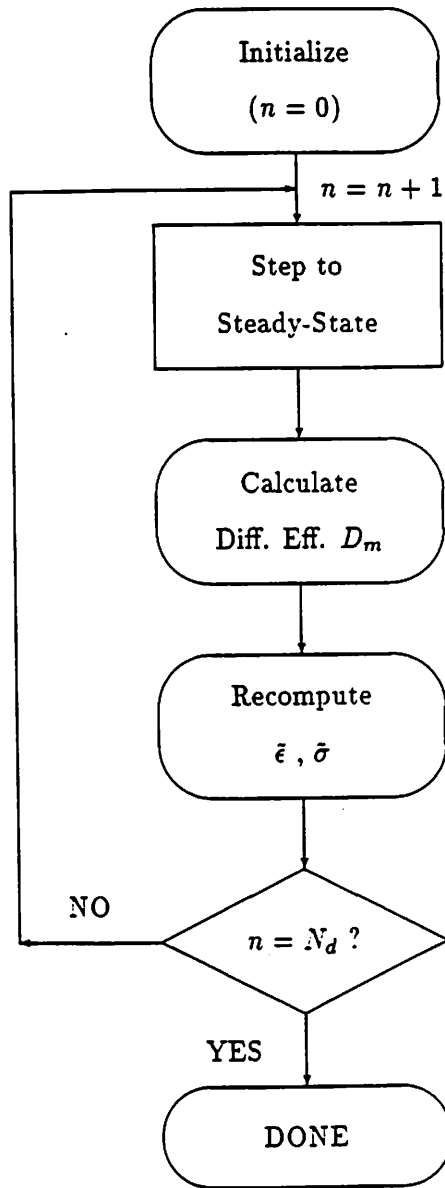
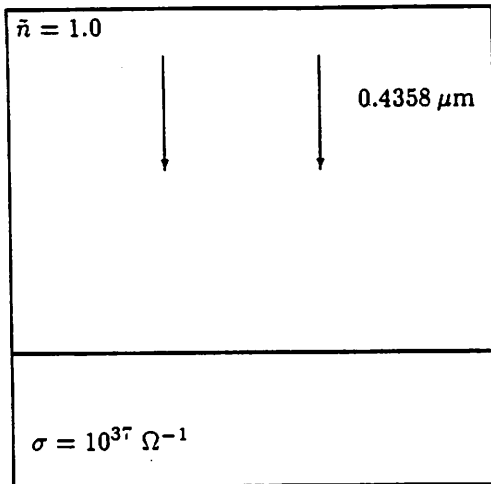
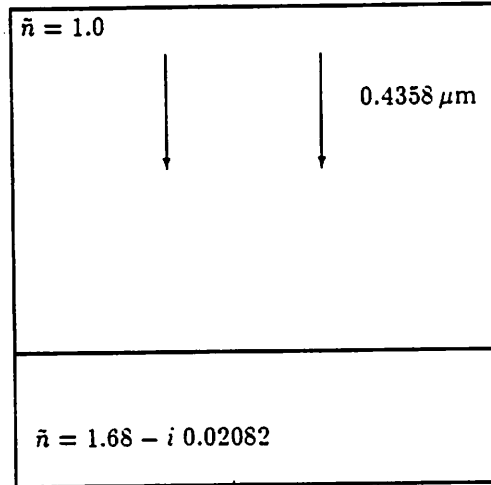


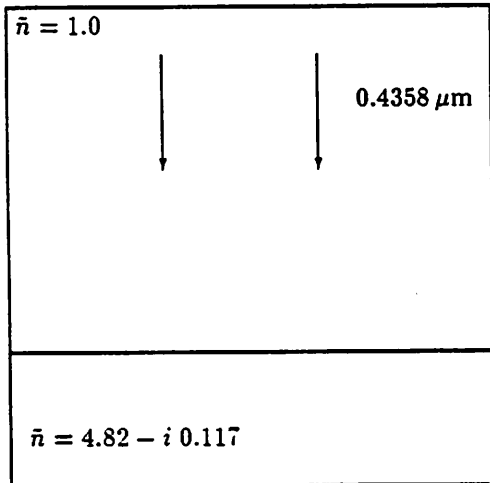
Figure 8: Flowchart for simulation of dynamic photoresist bleaching.



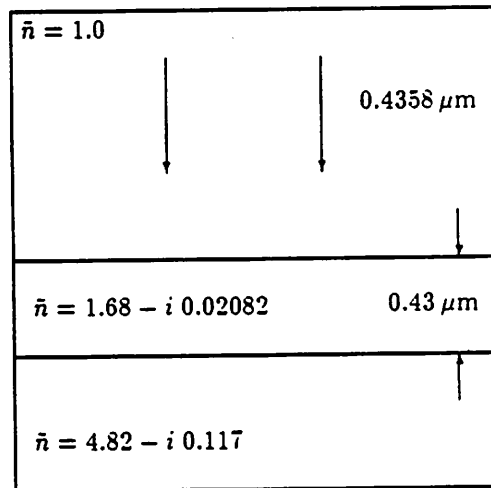
PERFECT CONDUCTOR



RESIST



SILICON



SILICON/RESIST

Figure 9: Planar dielectric structures for testing the inherent limits of the algorithm. Absorbing boundary conditions are applied $0.2 \mu\text{m}$ below the surface of the lowest material to emulate infinite thickness.

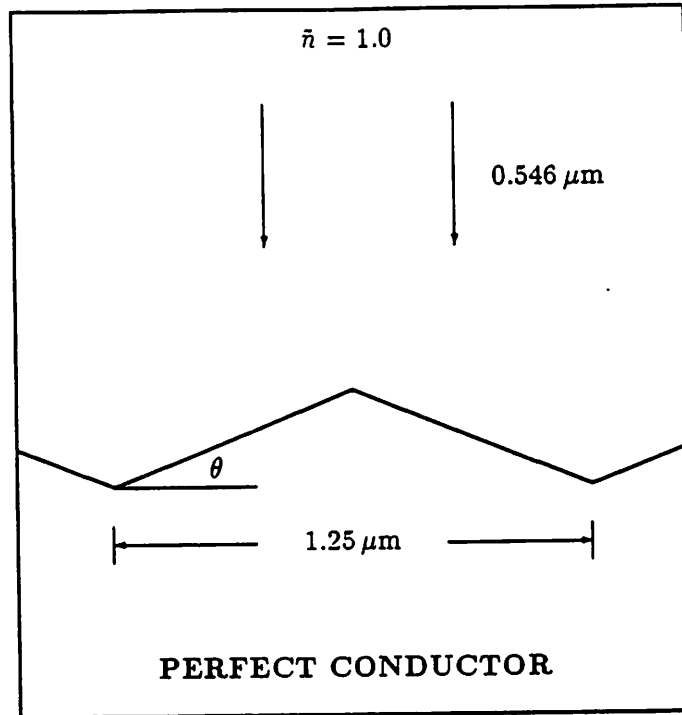


Figure 10: Symmetric perfectly conducting grating of Petit and Kalhor [30].

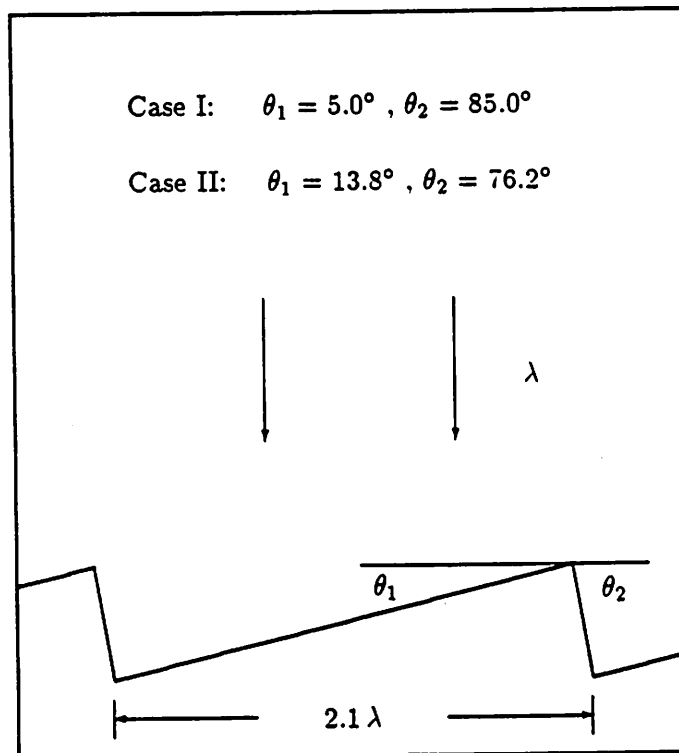


Figure 11: Schematic of asymmetric echelle grating for diffraction efficiency calculations.

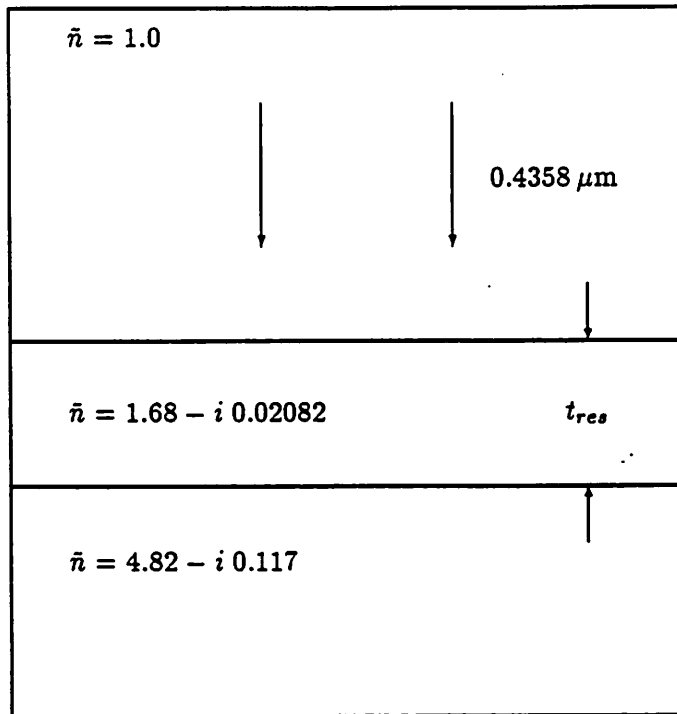


Figure 12: Layer structure for flat substrate exposure.

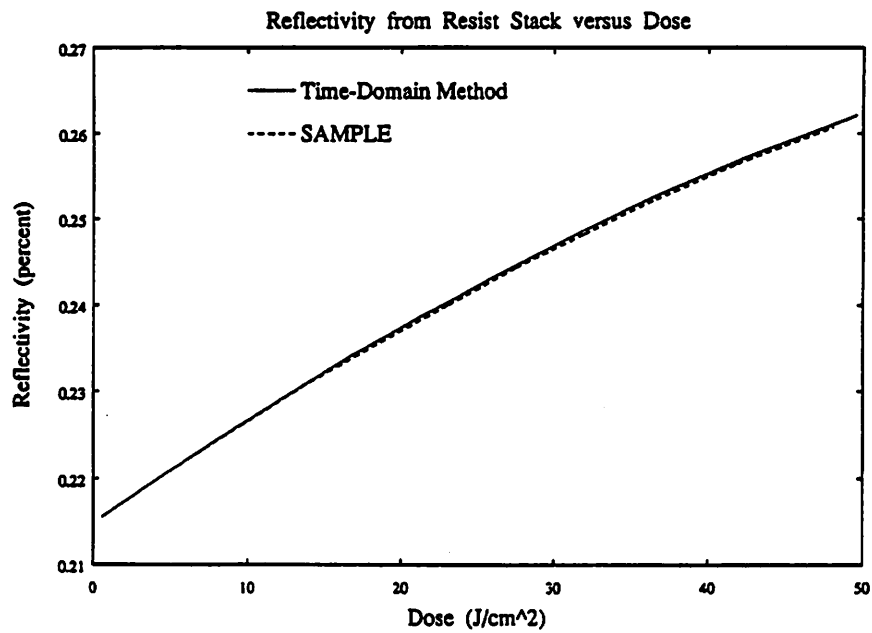


Figure 13: Comparison of reflectivity vs dose for the structure of Figure 12 at the condition of maximum thickness sensitivity ($t_{res} = 5.5\lambda/4$).

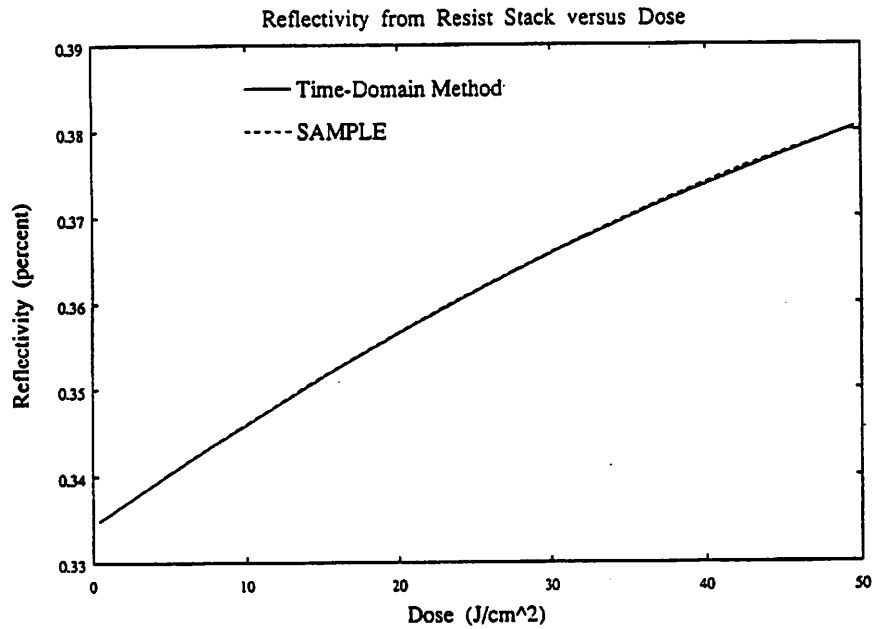


Figure 14: Comparison of reflectivity vs dose for the structures of Figure 12 at the condition of minimum thickness sensitivity ($t_{res} = 6.0\lambda/4$).

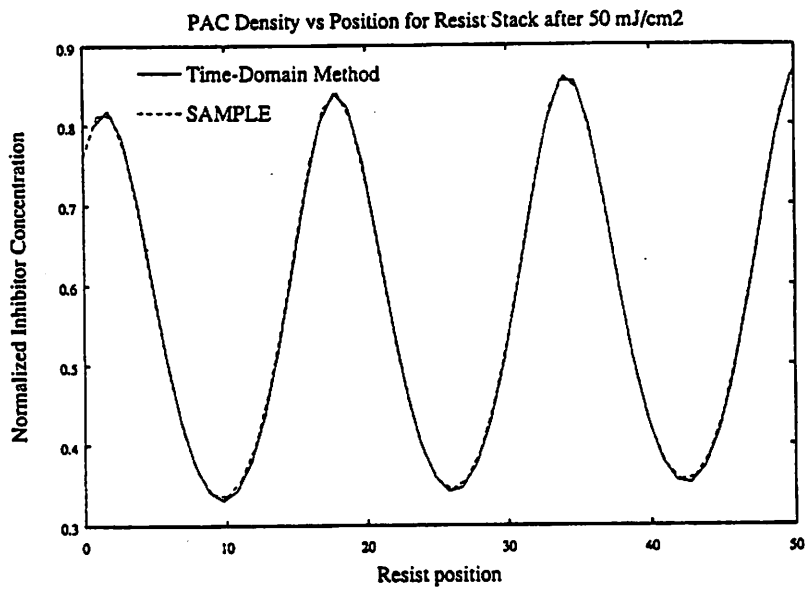


Figure 15: Comparison of the photosensitizer distribution obtained by the time domain method with calculations by SAMPLE throughout a $0.405\mu\text{m}$ resist (Figure 12) after exposure to a dose of 50 mJ/cm^2 .

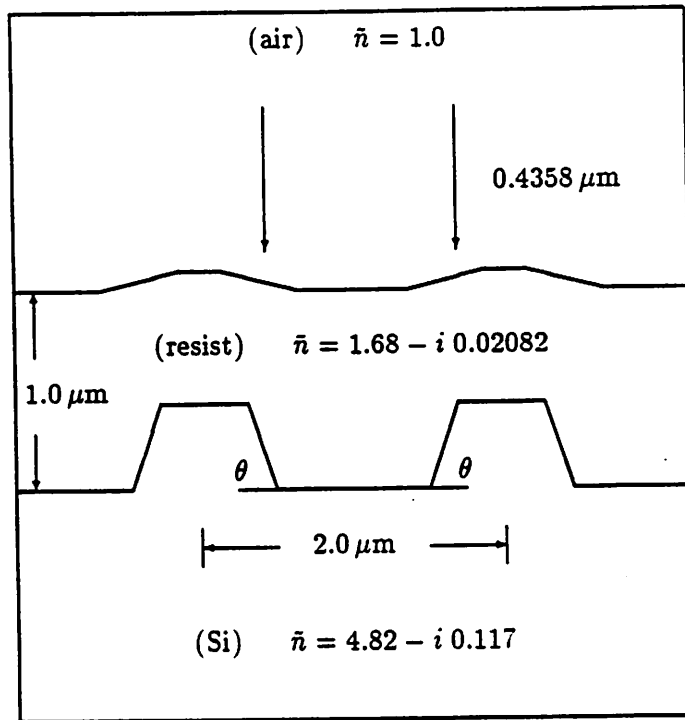


Figure 16: Example alignment grating for analysis of scattering from resist coating and substrate.

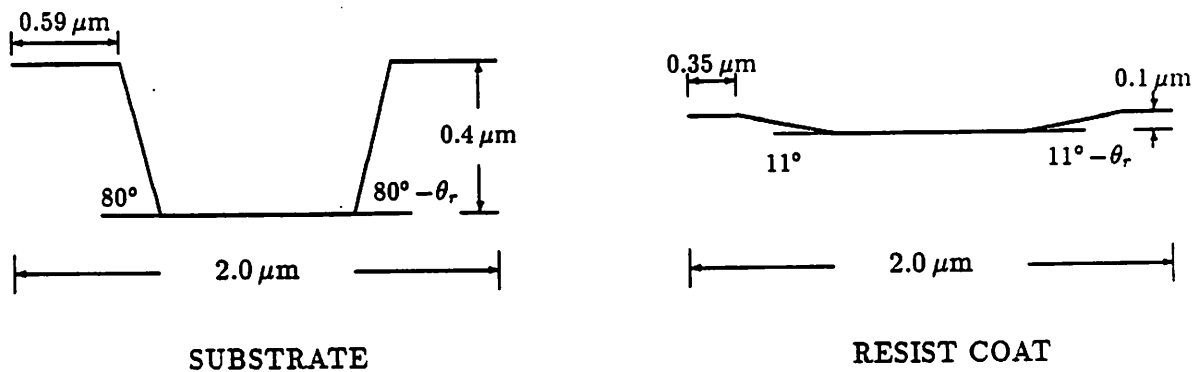


Figure 17: Models for the substrate and resist coating for the alignment example of Figure 16.

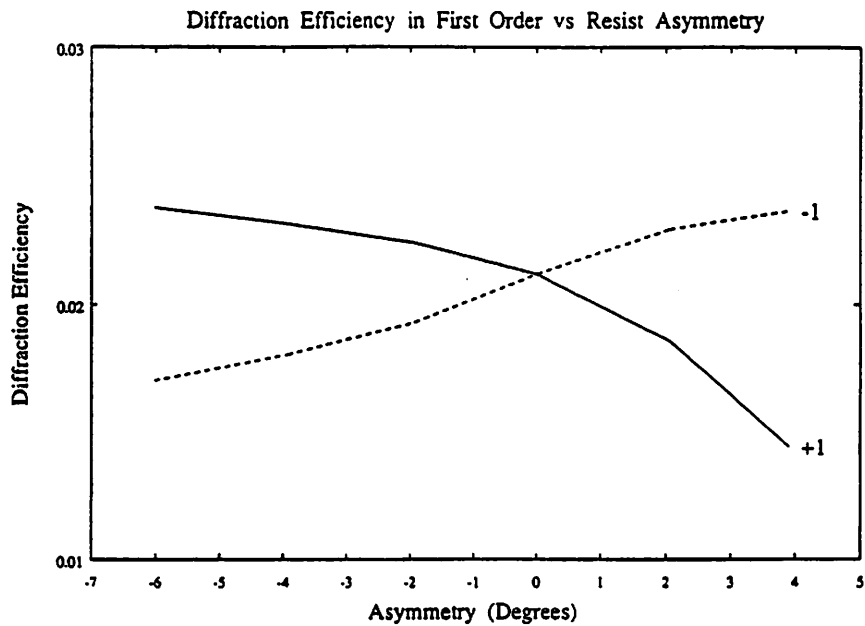


Figure 18: Plot of the diffraction efficiency in first order as a function of resist layer asymmetry. In the calculations, the resist is assumed to be infinite in thickness with the configuration shown in Figure 17.

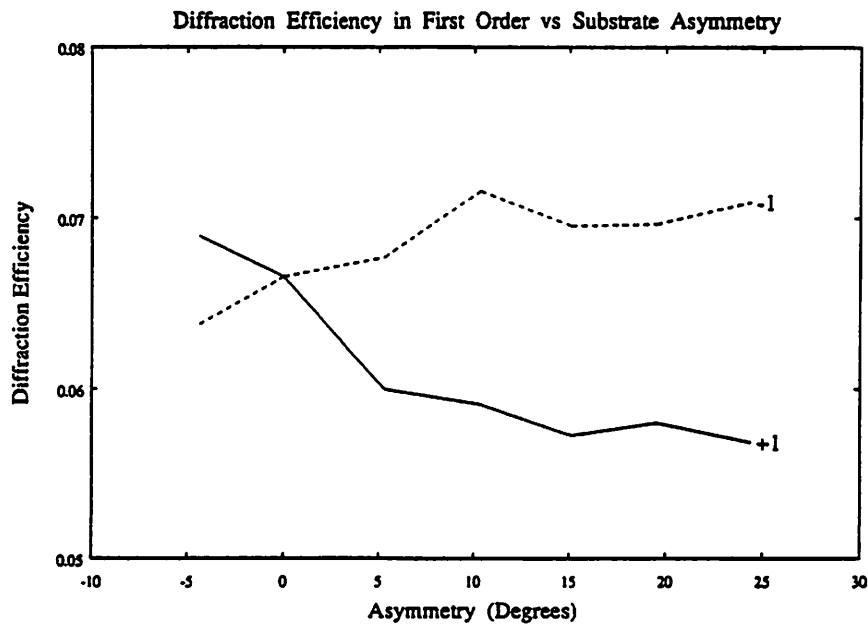


Figure 19: Plot of the diffraction efficiency in first order as a function of substrate asymmetry. In the calculations, the silicon substrate is assumed to be infinite in thickness with the configuration shown in Figure 17.

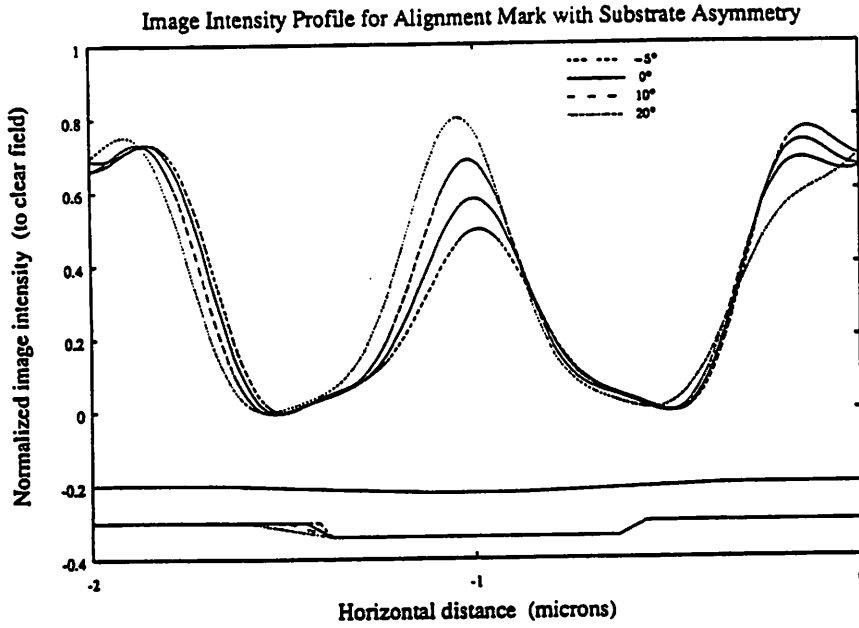


Figure 20: Illustration of the far-field image of the alignment mark of Figures 16 and 17 with substrate asymmetry. The incident field is a normally incident plane wave ($\lambda = 0.488\mu\text{m}$) and the resist is lossless ($\bar{n} = 1.68$). A scaled profile of the structure is provided to highlight the positions of the edges with asymmetry.

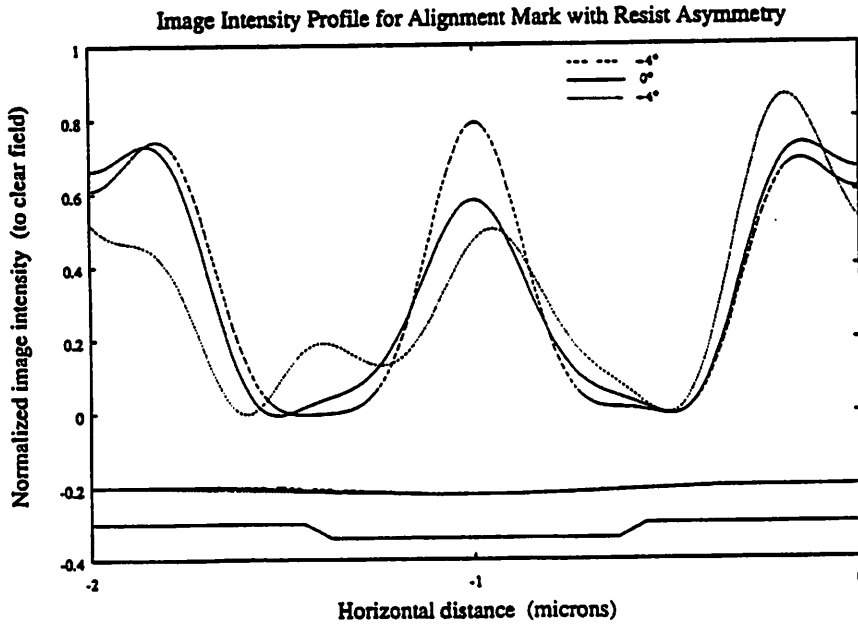


Figure 21: Illustration of the far-field image of the alignment mark of Figures 16 and 17 with resist asymmetry.

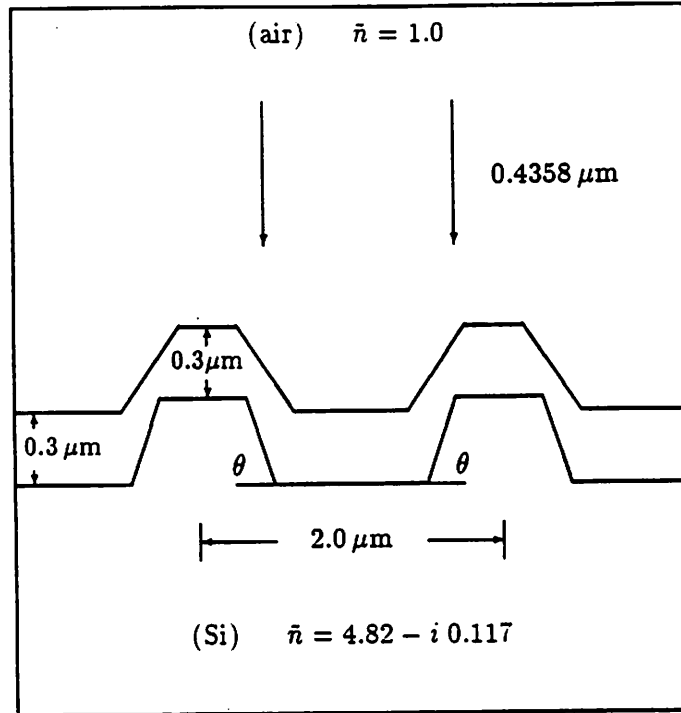


Figure 22: Alignment grating with interpenetrating resist coating.

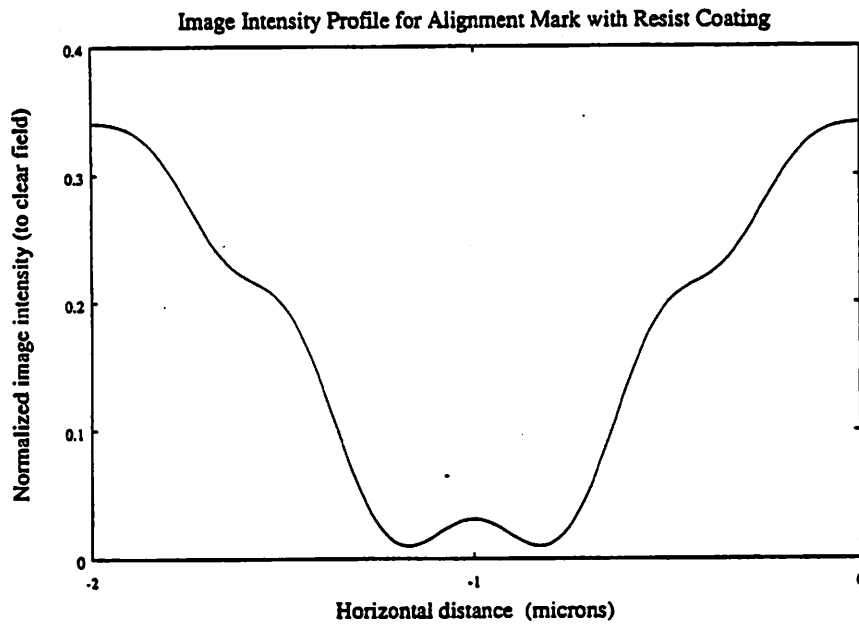


Figure 23: Far-field image of the alignment mark of Figure 22 for a resist with $\bar{n} = 1.68 - i 0.02082$.

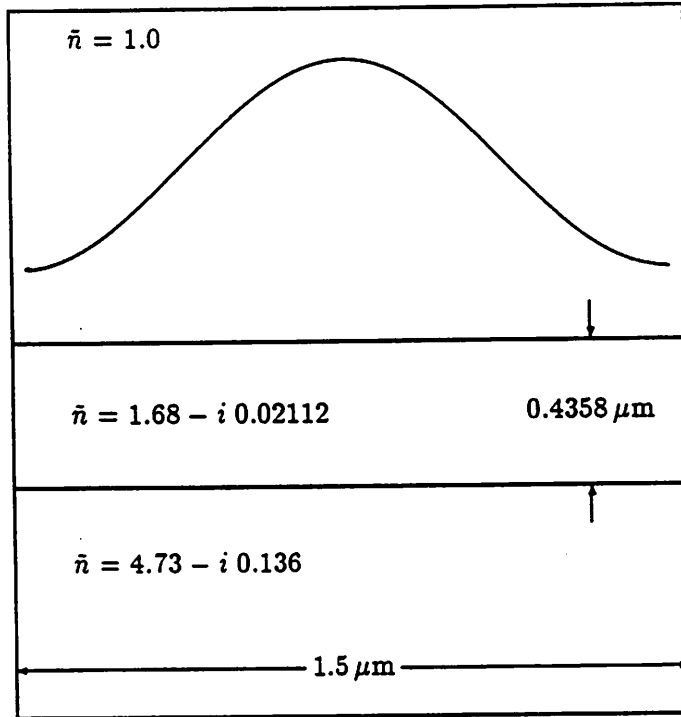


Figure 24: Dielectric layers and image used for latent image diffraction simulations.

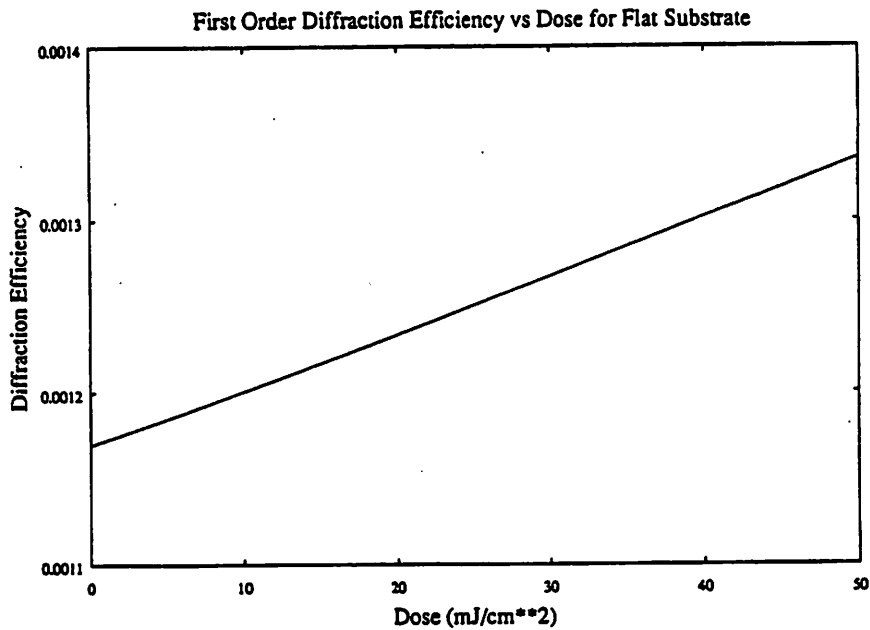


Figure 25: Simulated first order diffraction efficiencies for the exposure illustrated by Figure 24. The power for this case rises linearly with exposure dose. Table V summarizes the simulation parameters including the SAMPLE inputs used for calculation of the aerial image.

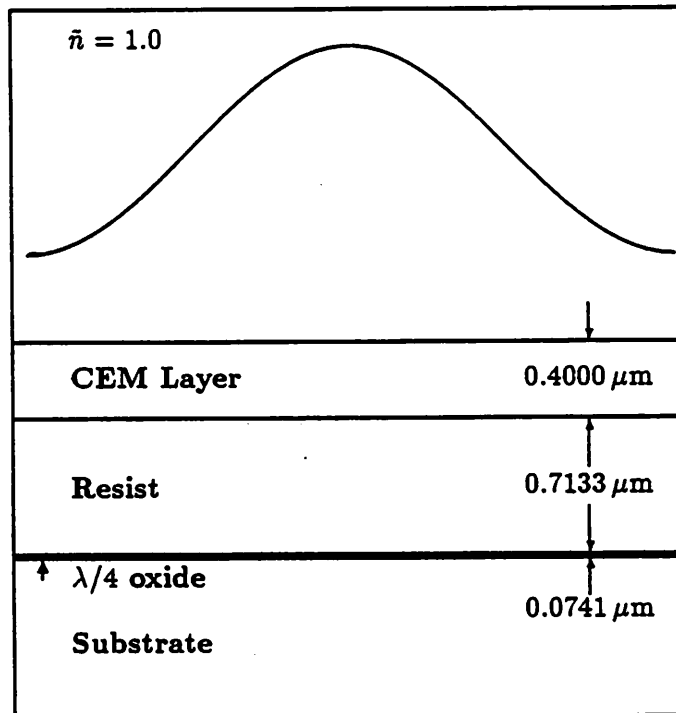


Figure 26: Layer structure for CEM exposure.

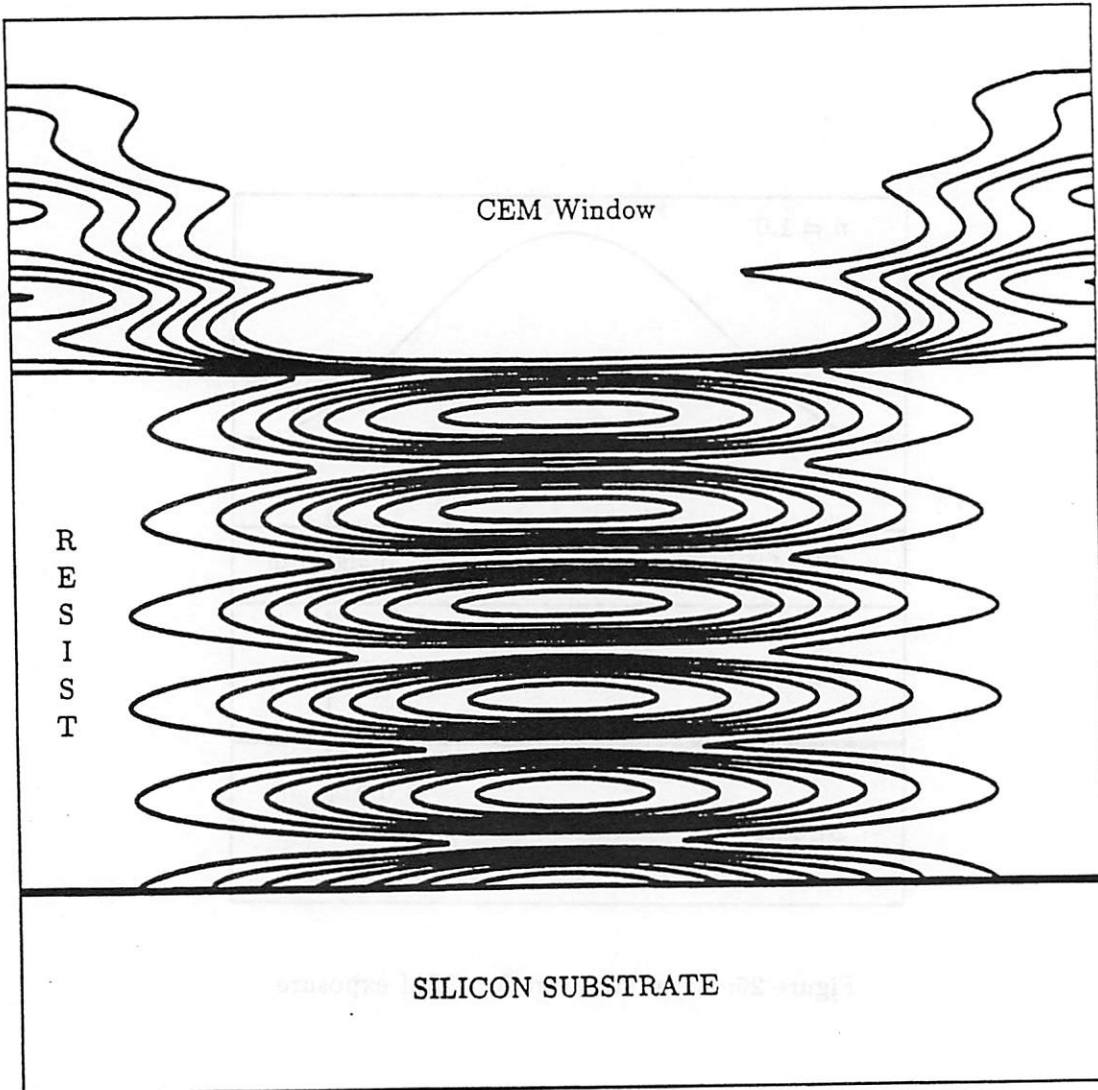
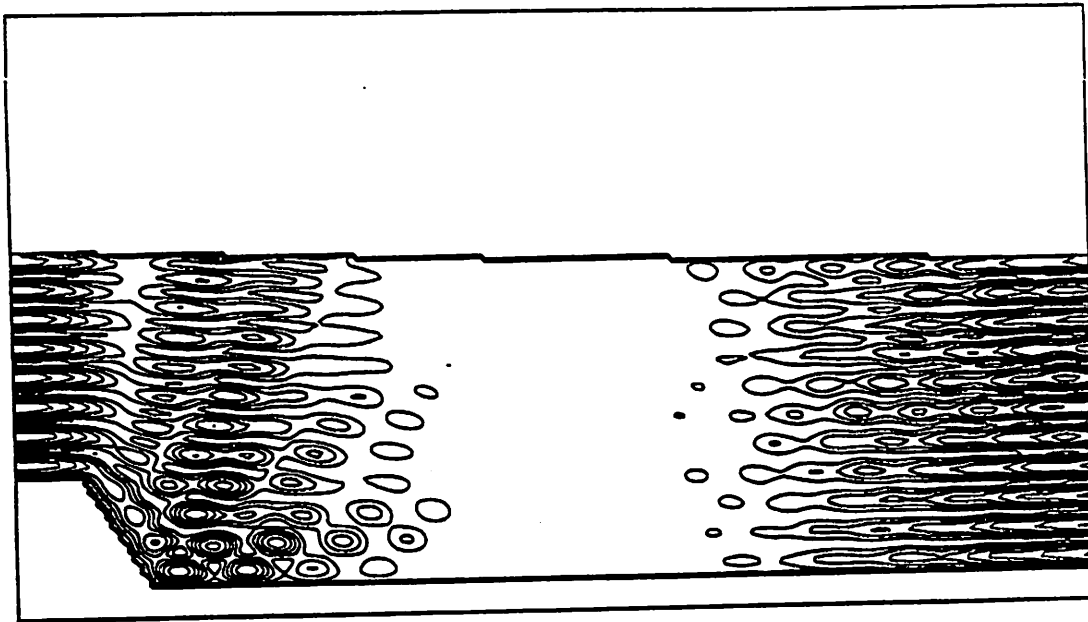
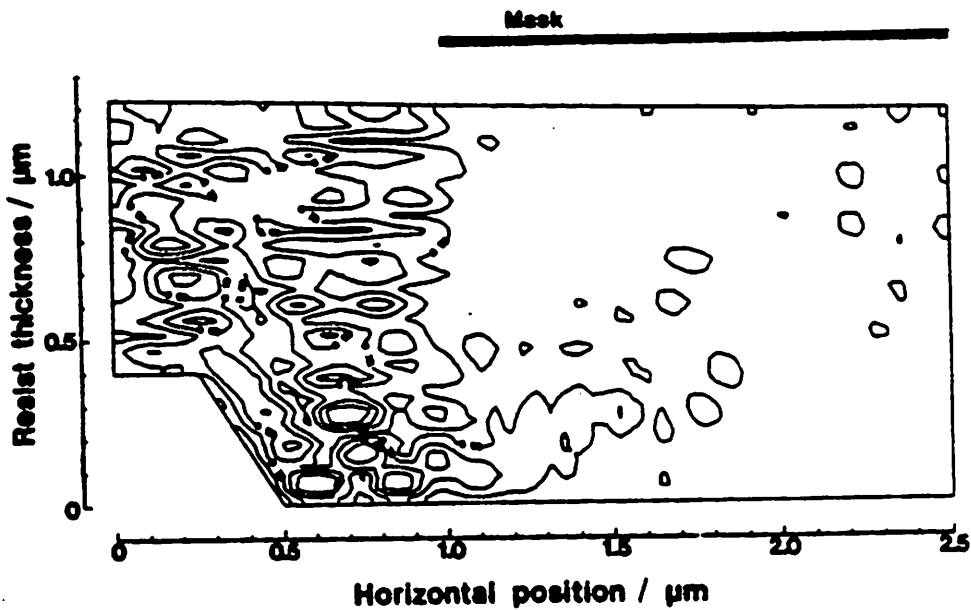


Figure 27: Inhibitor distribution contours for the CEM exposure illustrated by Figure 26. Table VI summarizes the simulation parameters including the SAMPLE inputs used for calculation of the aerial image.

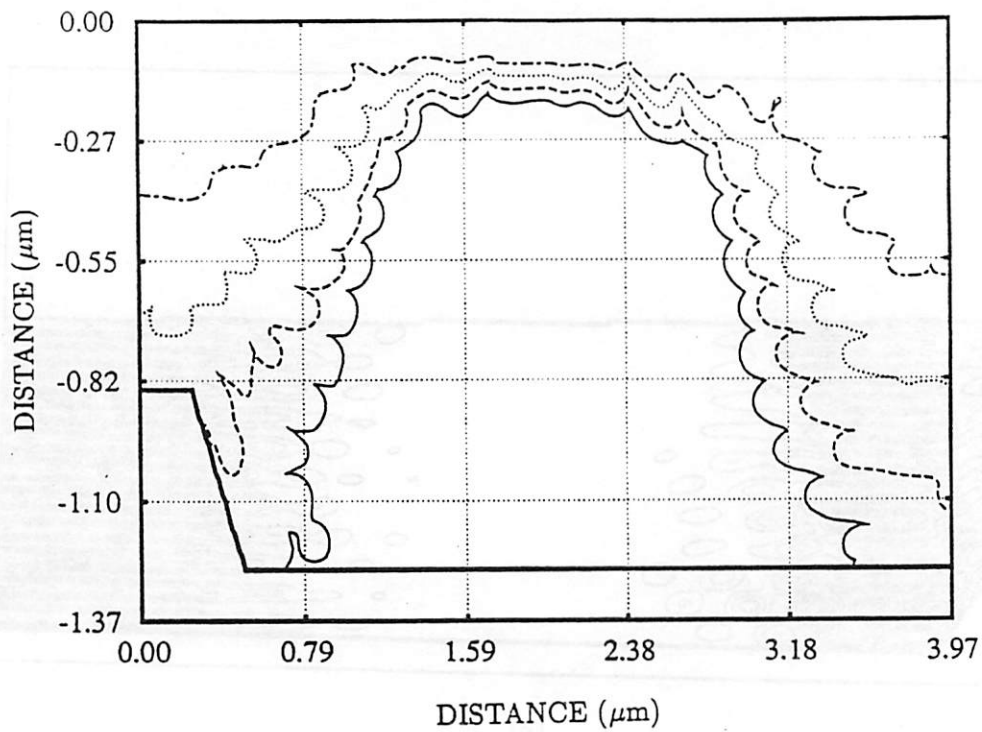


(a)

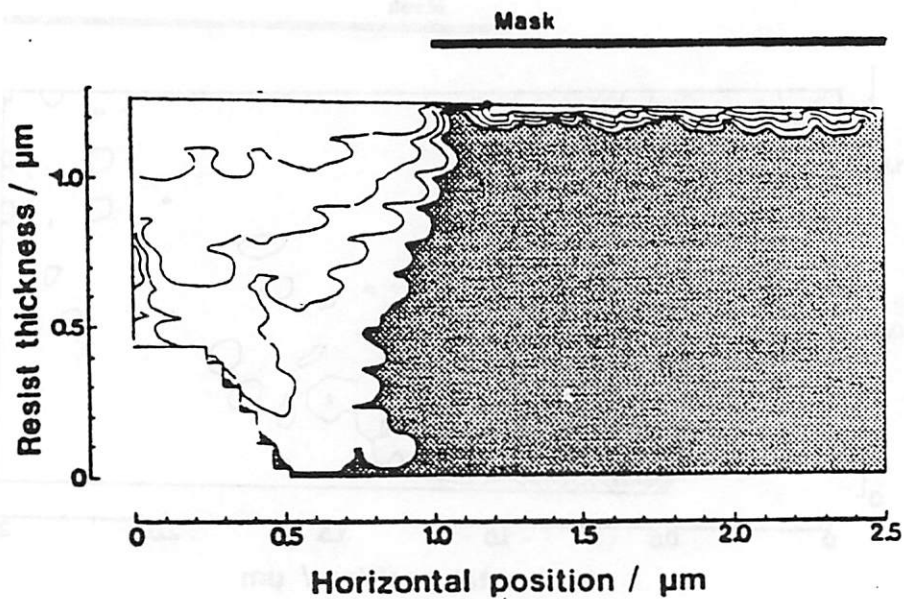


(b)

Figure 30: Inhibitor distribution contours produced by the (a) time-domain and (b) hybrid finite element methods for the exposure over a stepped substrate illustrated by Figure 29. The interval between contours is 0.2.

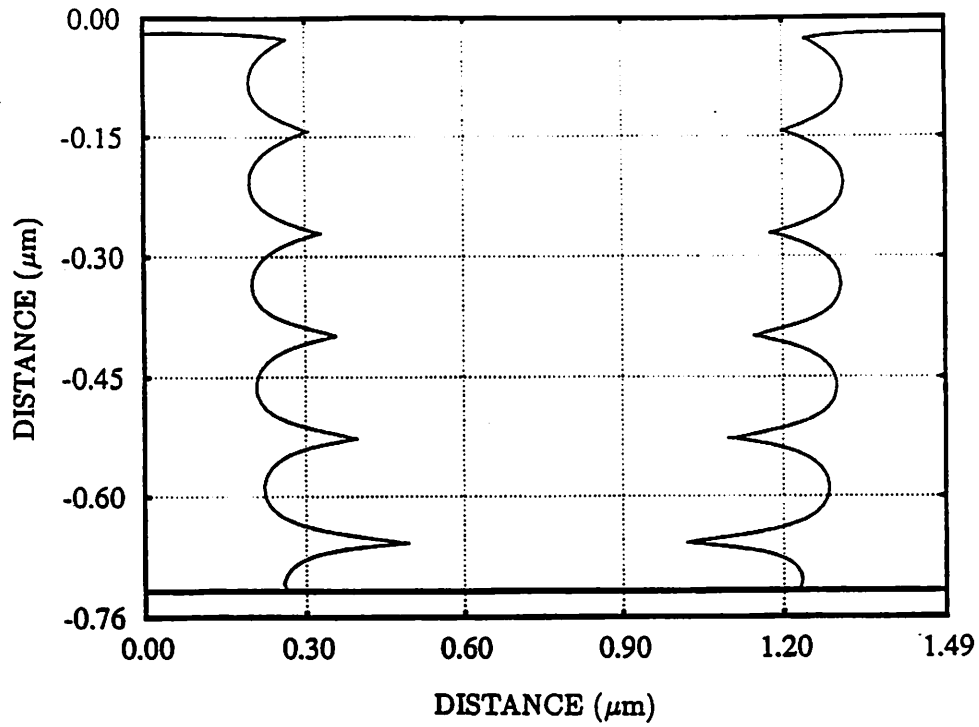


(a)

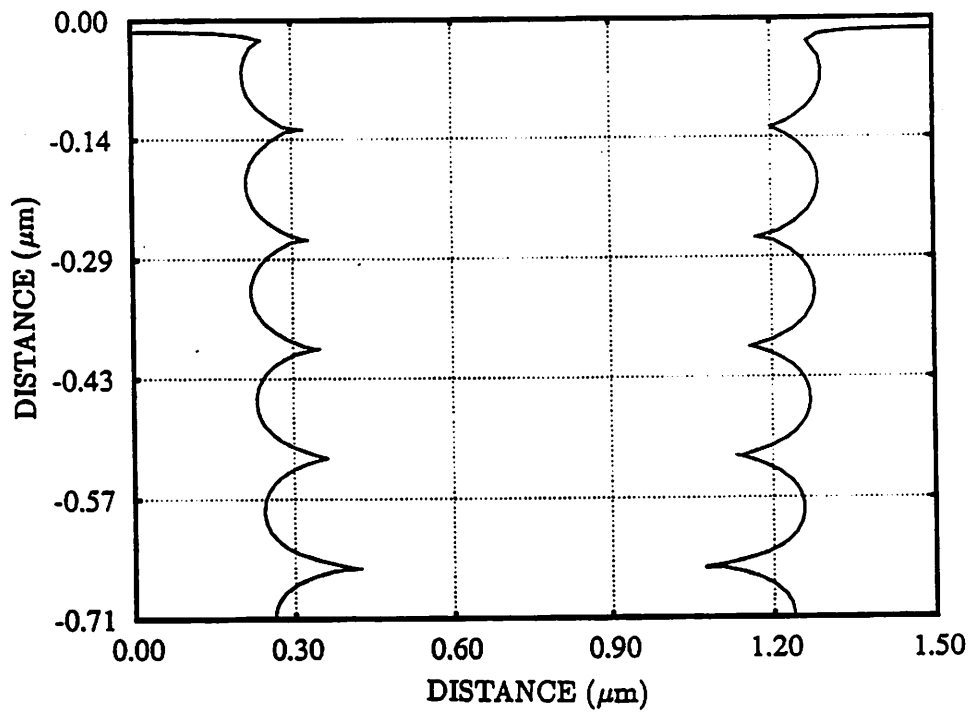


(b)

Figure 31: Simulated development profiles for the photosensitizer contours of Figure 30. Profile curves are drawn for 10 second intervals during the 40 second development for the hybrid finite element method (b) and for 20 second intervals in the 80 second development for the time-domain method (a).



(a)



(b)

Figure 28: Development contours produced by SAMPLE for the CEM exposure illustrated by Figure 26 after 80 seconds development: (a) Time-domain results. (b) SAMPLE profiles.

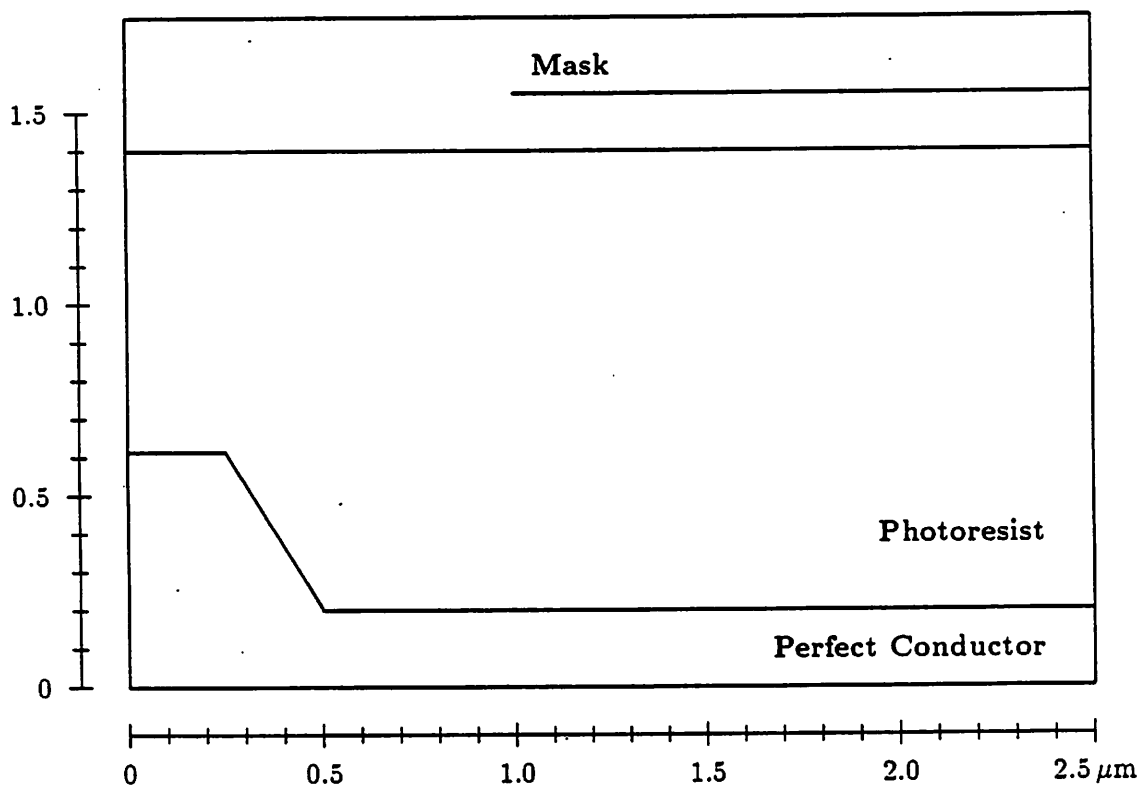


Figure 29: Reflective stepped substrate used by Matsuzawa et al. [13] with the hybrid finite element method. The photoresist surface has a gradual slope across the step which was approximated by a straight line with a slope of -2.0° from 0 to $2.5 \mu\text{m}$ and -1.0° out to the boundary at $4.0 \mu\text{m}$ (not shown). The height of the resist at the left boundary is $1.342 \mu\text{m}$.

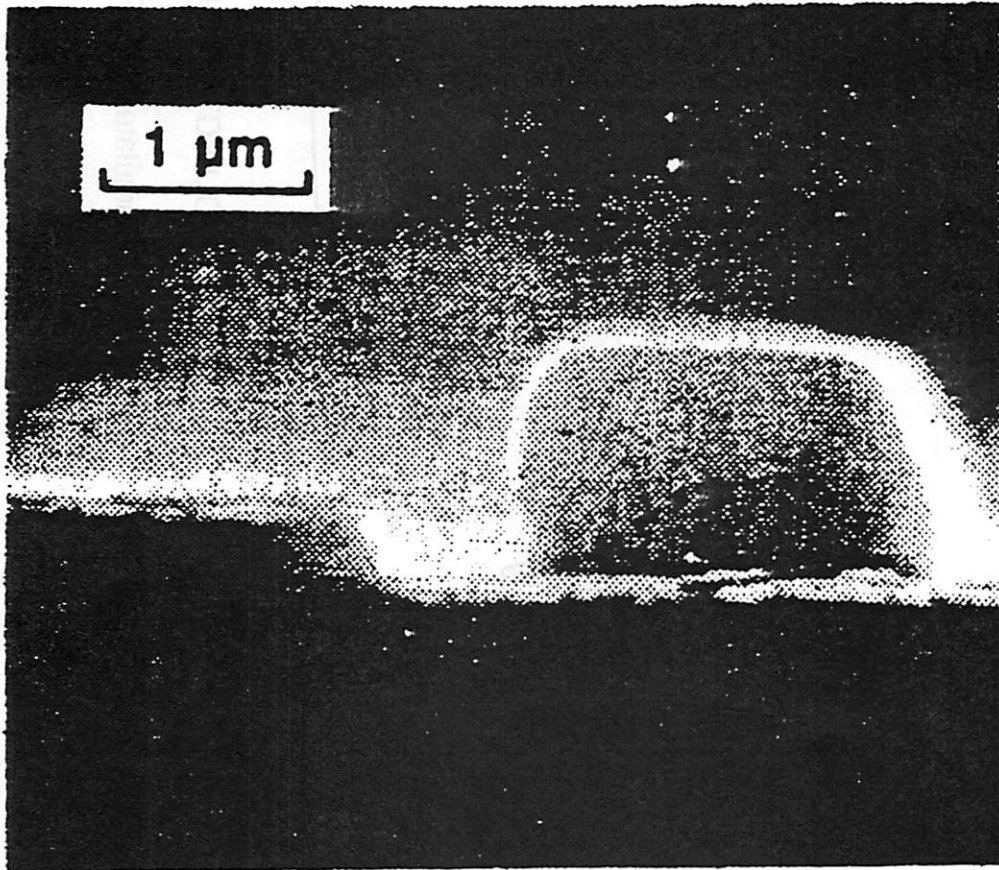


Figure 32: Scanning electron micrograph (SEM) of actual photoresist profile remaining on stepped substrate with $0.1 \mu\text{m}$ aluminum coating. (From reference [13]).

UNFOLDED REPRESENTATION OF OPTICAL SYSTEM

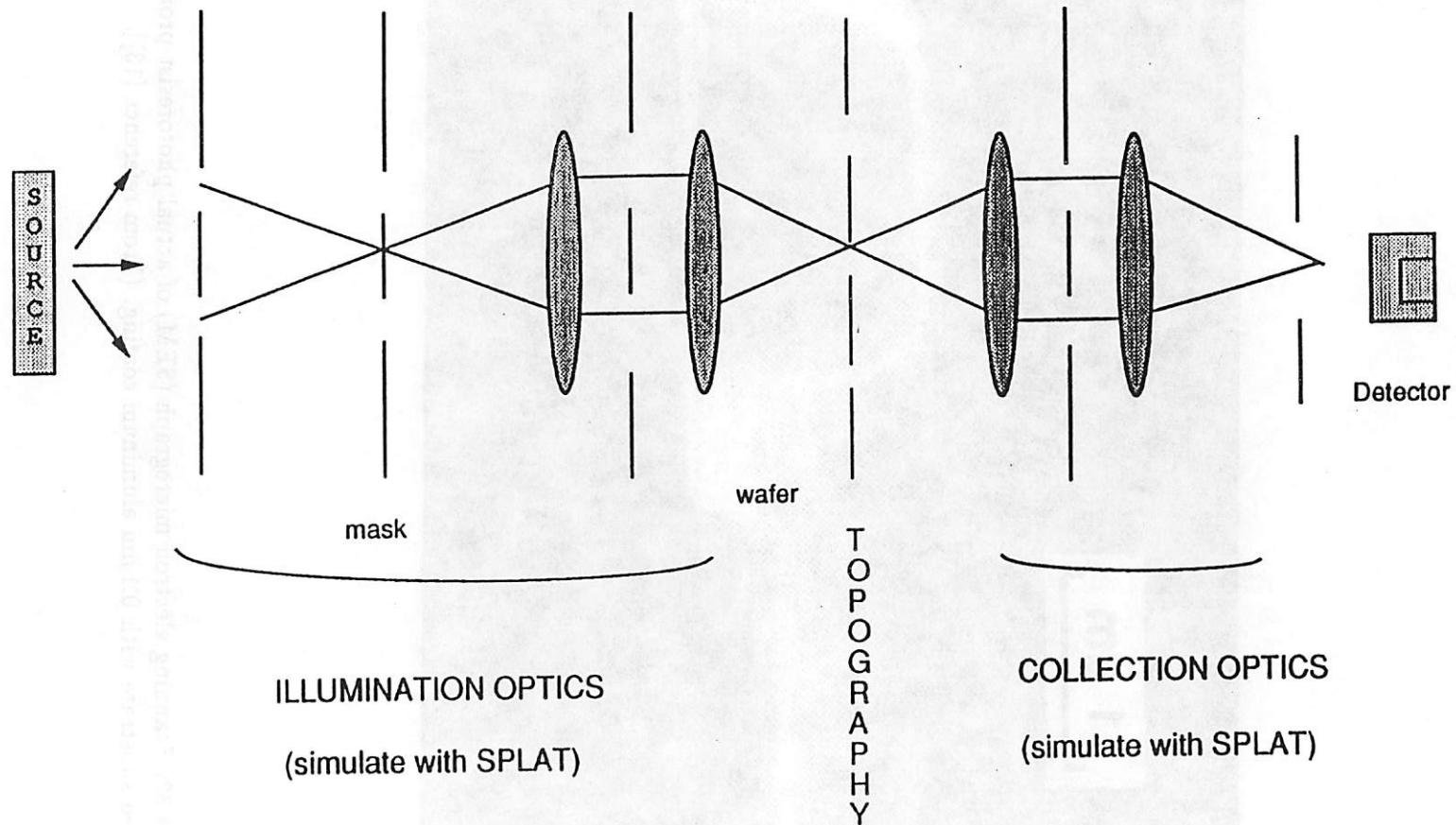


Figure 33: Unfolded representation of a typical optical lithography system. The collection optics usually capture scattered fields outside the aperture of the illumination optics.

APPENDICES

Appendix A — Outline of Diffraction Efficiency Calculations

Appendix B — Example Connection Machine Code

Appendix A

This appendix outlines the method for determining the coefficients of the scattered far-field for reconstruction or diffraction efficiency calculations. Expanding the scattered field in outgoing harmonics,

$$\begin{aligned}
 f_s(\vec{r}, t) &= \sum_n \left\{ A_n \cos(\omega t - \vec{k}_n \cdot \vec{r}) + B_n \sin(\omega t - \vec{k}_n \cdot \vec{r}) \right\} \\
 &= \sum_n \left\{ A_n \left[\cos(\omega t) \cos(\vec{k}_n \cdot \vec{r}) + \sin(\omega t) \sin(\vec{k}_n \cdot \vec{r}) \right] \right. \\
 &\quad \left. + B_n \left[\sin(\omega t) \cos(\vec{k}_n \cdot \vec{r}) - \cos(\omega t) \sin(\vec{k}_n \cdot \vec{r}) \right] \right\} \quad (52)
 \end{aligned}$$

Consider two times t_1 and t_2 such that $\cos(\omega t_1) = 0$ and $\sin(\omega t_2) = 0$ and suppose that the scattered field is known along C-D for the case of Figure 1. Evaluating (52) at $t = t_1$, multiplying both sides by $\sin(\vec{k}_m \cdot \vec{r})$, and integrating over the top surface ($x = x_0$) we have

$$\begin{aligned}
 \int f_s(\vec{r}, t_1) \sin(\vec{k}_m \cdot \vec{r}) dy &= \sum_n \left\{ A_n \int \sin(\vec{k}_n \cdot \vec{r}) \sin(\vec{k}_m \cdot \vec{r}) dy + B_n \int \cos(\vec{k}_n \cdot \vec{r}) \sin(\vec{k}_m \cdot \vec{r}) dy \right\} \\
 &= \frac{1}{2} \sum_n \left\{ A_n \int \cos[(\vec{k}_n - \vec{k}_m) \cdot \vec{r}] - \cos[(\vec{k}_n + \vec{k}_m) \cdot \vec{r}] dy \right. \\
 &\quad \left. + B_n \int \sin[(\vec{k}_m - \vec{k}_n) \cdot \vec{r}] + \sin[(\vec{k}_m + \vec{k}_n) \cdot \vec{r}] dy \right\} \quad (53)
 \end{aligned}$$

which from orthogonality reduces to

$$\begin{aligned}
 \gamma_{11} &= \int_{C-D} f_s(\vec{r}, t_1) \sin(\vec{k}_m \cdot \vec{r}) dy \\
 &= \frac{d}{2} [A_m - \cos(2k_{mx}x_0)A_{-m} + \sin(2k_{mx}x_0)B_{-m}] \quad (54)
 \end{aligned}$$

where d is the period and k_{mx} is the x component of the propagation constant of the m th outgoing mode. If we perform the same operations with $\cos(\vec{k}_m \cdot \vec{r})$, we get a similar result

$$\begin{aligned}
 \gamma_{12} &= \int_{C-D} f_s(\vec{r}, t_1) \cos(\vec{k}_m \cdot \vec{r}) dy \\
 &= \frac{d}{2} [B_m + \cos(2k_{mx}x_0)B_{-m} + \sin(2k_{mx}x_0)A_{-m}] \quad (55)
 \end{aligned}$$

Repeating the previous manipulations with (35) evaluated at time t_2 gives

$$\begin{aligned}\gamma_{21} &= \int_{C-D} f_s(\vec{r}, t_2) \sin(\vec{k}_m \cdot \vec{r}) dy \\ &= \frac{d}{2} [-B_m + \cos(2k_{mx}x_0)B_{-m} + \sin(2k_{mx}x_0)A_{-m}]\end{aligned}\quad (56)$$

$$\begin{aligned}\gamma_{22} &= \int_{C-D} f_s(\vec{r}, t_2) \cos(\vec{k}_m \cdot \vec{r}) dy \\ &= \frac{d}{2} [A_m + \cos(2k_{mx}x_0)A_{-m} - \sin(2k_{mx}x_0)B_{-m}]\end{aligned}\quad (57)$$

Relations (54) through (57) yield four equations in the four unknowns A_m , B_m , A_{-m} , and B_{-m} which can be solved to give

$$A_m = \frac{1}{d} [\gamma_{11} + \gamma_{22}] \quad (58)$$

$$B_m = \frac{1}{d} [\gamma_{12} - \gamma_{21}] \quad (59)$$

$$A_{-m} = \frac{\sin(2k_{mx}x_0)}{d} (\gamma_{21} + \gamma_{12}) - \frac{\cos(2k_{mx}x_0)}{d} (\gamma_{11} - \gamma_{22}) \quad (60)$$

$$B_{-m} = \frac{\cos(2k_{mx}x_0)}{d} (\gamma_{21} + \gamma_{12}) + \frac{\sin(2k_{mx}x_0)}{d} (\gamma_{11} - \gamma_{22}) \quad (61)$$

Using the convention of Figure 7, $x_0 = 0$ at the top boundary so the last two equations reduce to

$$A_{-m} = \frac{1}{d} [\gamma_{22} - \gamma_{11}] \quad (62)$$

$$B_{-m} = \frac{1}{d} [\gamma_{12} + \gamma_{21}] \quad (63)$$

Appendix B

Example Connection Machine Code

To establish a perspective of the programming environment of a massively parallel architecture such as the Connection Machine, this appendix presents example code written for the primary time domain loop of the algorithm. The syntax corresponds to version 5.0 of the Connection Machine *LISP software and is very similar to CommonLisp with a few modifications and extensions appropriate to control of multiple processor systems. All commands which are followed by !! are functions which are performed by all active processors in parallel. To subselect different sets of processors, to update boundary nodes for example. conditional tests such as **if* and **cond* are carried out on boolean flag variables (*pvars*) stored in each processor. If the evaluated expression produces a "false" response (nil), the processor is removed from the currently selected set and the commands within the scope of the statement are not performed.

In addition, intrinsic mapping functions such as *self-address-grid!!*, *news!!*, and **news!!* permit selection of processors with particular grid coordinates and local fetches/stores in the context of the *NEWS* system (discussed in Section 2.2), respectively. With these building blocks, groups of processors can be manipulated to carry out standard CommonLisp-like operations in an organized and flexible fashion. It should be pointed out that the system supports parallel versions of other high-level languages such as C and Fortran as well as its own assembly level language. More details can be found in the Connection Machine programming reference manuals.

89/05/16
17:37:06

example.cm.code

1

```
;; -*- Font: CPTFONT; mode: lisp; syntax: common-lisp; package: *lisp-cl; base: 10; -*-  
;;;  
;;; Declaration of the package is required here  
(in-package '*lisp)  
;;;  
;;; Pvar declarations  
;;;  
;; e      = electric field along z coordinate  
;; hx     = component of the magnetic field along x direction  
;;         having coordinates (i, j+1/2)  
;; hy     = component of the magnetic field along y direction  
;;         having coordinates (i+1/2, j)  
;;;  
;;;  
(*proclaim '(type (pvar single-float) e hx hy))  
(*defvar e  (!! 0.0))  
(*defvar hx (!! 0.0))  
(*defvar hy (!! 0.0))  
;;;  
;;; Multiplicative values needed by the algorithm  
;;;  
(*proclaim '(type (pvar single-float) alpha beta))  
(*defvar alpha (!! 0.0))  
(*defvar beta  (!! 0.0))  
;;;  
;;; Optical index and resist sensitizer concentration  
;;;  
(*proclaim '(type (pvar single-float) n mm))  
(*defvar n  (!! 0.0))  
(*defvar mm (!! 0.0))  
;;;  
;;; Local scratch memory location  
;;;  
(*proclaim '(type (pvar single-float) reg))  
(*defvar reg (!! 0.0))  
;;;  
;;; This flag is true when a processor belongs to one  
;;; of the dummy layers. The top layer is used for  
;;; updating h fields and the lower for e fields  
;;;  
(*proclaim '(type (pvar boolean) dummy-layer-north inc fields))  
(*defvar dummy-layer-north nil!!)  
(*defvar inc fields nil!!)  
;;;  
;;; These flags are true when a processor belongs to the boundary layers  
;;;  
(*proclaim '(type (pvar boolean) boundary-north boundary-south boundary))  
(*defvar boundary-north nil!!)  
(*defvar boundary-south nil!!)  
(*defvar boundary      nil!!)  
;;;  
;;; This flag true when layer-resist  
;;;  
(*proclaim '(type (pvar boolean) resist resist cel))  
(*defvar resist nil!!)  
(*defvar resist cel nil!!)  
;;;  
;;; Flag designating top layer for diffraction efficiency calculations  
;;;  
(*proclaim '(type (pvar boolean) top-layer))  
(*defvar top-layer nil!!)  
;;;  
;;; This flag is true when the processor is not associated with  
;;; a dummy node
```

```
;;;  
(*proclaim '(type (pvar boolean) simulation-domain))  
(*defvar simulation-domain nil!!)  
;;;  
;;; Scratch flags  
;;;  
(*proclaim '(type (pvar boolean) err_test  
simulation-domain-not-south simulation-domain-not-north))  
(*defvar simulation-domain-not-north nil!!)  
(*defvar simulation-domain-not-south nil!!)  
(*defvar err_test nil!!)  
;;;  
;;; Integration time and spatial discretization interval  
;;;  
(proclaim '(type single-float dx dt))  
(defvar dx 0.0)  
(defvar dt 0.0)  
;;;  
;;; Wave parameters  
;;;  
(proclaim '(type single-float amplitude kx omega gammaf delta))  
(defvar amplitude 0.0)  
(defvar kx 0.0)  
(defvar omega 0.0)  
(defvar gammaf 0.0)  
(defvar delta 0.0)  
;;;  
;;; Discretization steps along y-direction and x-direction  
;;;  
(proclaim '(type fixnum *y-dimension* *x-dimension* *x-dimension*-1  
*y-dimension*-1))  
(defvar *y-dimension* 64)  
(defvar *x-dimension* 64)  
(defvar *x-dimension*-1 63)  
(defvar *y-dimension*-1 63)  
;;;  
;;;;;;;;;;;;;;;;;;;;;;;;;;;;;;;;;;;;;;;;;;;;;;;;;;;;;;;;;;;;;;;;;;;;;;;;;;;;;;;;  
;;;  
;;; Computation of the value of the flags  
;;;  
;;;;;;;;;;;;;;;;;;;;;;;;;;;;;;;;;;;;;;;;;;;;;;;;;;;;;;;;;;;;;;;;;;;;;;;;;;;;;;;;  
;;;  
(defun set-flags ()  
  
  (*set boundary-north  nil!!)  
  (*set boundary-south  nil!!)  
  (*set boundary        nil!!)  
  (*set simulation-domain nil!!)  
  (*set dummy-layer-north nil!!)  
  (*set simulation-domain-not-north nil!!)  
  (*set simulation-domain-not-south nil!!)  
  (*set top-layer       nil!!)  
  (*set inc fields      nil!!)  
  (*set err test        nil!!)  
  
  (*if (-!! (self-address-grid!! (!! 1)) (!! 10))  
    (*set err test (!!))  
  )  
  
  )  
;;;  
;;;  
;;; The processors associated with the boundary conditions are  
;;; selected now  
;;;
```


89/05/16
17:37:06

example.cm.code

3

```
;;; boundary conditions and the incident field are included.
;;;
;;;
;;; The computation of the incident field requires four multiplications
;;; and two additions.
;;; Referring to the variables defined in routine
;;;
;;; Initialize-boundary-conditions
;;;
;;; we have to compute the following operations:
;;;
;;; alpha = alpha*gamma - beta*e
;;; beta = beta*gamma + alpha*e
;;;
;;; Referring to the report, the following equivalence between
;;; the two coordinate systems holds:
;;;
;;; y (CM) x (REP)
;;; x (CM) -y (REP)
;;;
;;;
(defun inn-loop ()
  ;;
  ;; Computation of the new value of the magnetic field along y
  ;;
  (if simulation-domain-not-south
    (prog ()
      (*set reg (-!! (news!! e 0 1) e))
    )
    (if simulation-domain-not-north
      (if boundary-south
        (prog ()
          (*set reg (!!! (!! cb2)
            (-!! (!!! (!! c6) (-!! (news!! hx 0 -1) (news!! hx 1 -1))) reg)))
          (*set reg (-!! (!!! (!! c6) (news!! e 0 -1)) (+!! reg (!!! (!! cb1) e))))
          (*set reg (-!! (+!! reg hy) (news!! hy 0 -1)))
        )
        (prog ()
          (*set reg (!!! (!! c2) (-!! (news!! hx 0 1) (+!! reg (news!! hx 1 1))))
          (*set reg (-!! (-!! (news!! e 0 1) beta) (+!! reg (!!! (!! c1) e))))
        )
      )
    )
  )
  ;;
  ;; Subtract off incident electric field
  ;;
  (if boundary-north
    (*set reg (-!! reg (news!! beta 0 -1)))
  )
  ;;
  ;; The following operations are not required along the south
  ;; boundary (but applied anyways) since absorbing boundary
  ;; conditions are locally applied to the e field and hy is
  ;; determined by the outgoing plane wave condition.
  ;;
  (*set hy (+!! hy (!!! reg (!! gamma))))
  )
  ;;
  ;; Computation of the new value of the magnetic field along x
  ;;
  (*set reg (-!! e (news!! e -1 0)))
  (*set hx (+!! hx (!!! (!! gamma) reg)))
  ;;
  ;;
  ;;
  ;; Computation of the electric field
  ;;
```

```
;;; The allocation of the variables in our scheme requires a different
;;; treatment of the south side of the domain to account for the
;;; outgoing wave/absorbing boundary conditions.
;;;
;;;
;;;
;;;
;;; (*set reg (-!! (news!! hx 1 0) hx))
;;;
;;;
;;;
;;; cb1,cb2 = c1,c2 for bottom boundary
;;;
;;; c6 = attenuation factor = exp(-alpha*dx)
;;;
;;;
;;;
;;;
;;; (*if simulation-domain-not-north
;;; (*if boundary-south
;;; (prog ()
;;; (*set reg (!!! (!! cb2)
;;; (-!! (!!! (!! c6) (-!! (news!! hx 0 -1) (news!! hx 1 -1))) reg)))
;;; (*set reg (-!! (!!! (!! c6) (news!! e 0 -1)) (+!! reg (!!! (!! cb1) e))))
;;; (*set reg (-!! (+!! reg hy) (news!! hy 0 -1)))
;;; )
;;; (prog ()
;;; (*set reg (!!! (!! c2) (-!! (news!! hx 0 1) (+!! reg (news!! hx 1 1))))
;;; (*set reg (-!! (-!! (news!! e 0 1) beta) (+!! reg (!!! (!! c1) e))))
;;; )
;;; )
;;;
;;;
;;; Update of the magnetic field for time n + 1/2 and nodes dx/2
;;; and electric field for time n+1.
;;;
;;;
;;;
;;; (*if inc_fields
;;; (prog ()
;;; (*set e (-!! (!!! alpha (!! gammaf)) (!!! beta (!! delta))))
;;; (*set beta (+!! (!!! beta (!! gammaf)) (!!! alpha (!! delta))))
;;; (*set alpha e)
;;; )
;;; (*set e (+!! (!!! beta reg) (!!! e alpha)))
;;; )
;;;
;;;
;;; Final stage of second order conditions for
;;; north/south boundaries
;;;
;;;
;;; (*if boundary-north
;;; (*set e (+!! reg (!!! (!! c1) (-!! (news!! e 0 1) beta))))
;;; )
;;;
;;; (*if boundary-south
;;; (*set e (+!! reg (!!! (!! cb3) (news!! e 0 -1))))
;;; )
;;; )
```

example.cm.code

```

;;;
;;; end of the routine
;;;
;;;;;;;;;;;;;;;;;;;;;;;;;;;;;;;;;;;;;;;;;;;;;;;;
;;;
;;; Inner time domain loop module for initial gaussian
;;; excitation.
;;;
;;;;;;;;;;;;;;;;;;;;;;;;;;;;;;;;;;;;;;;;;;;;;;;;
(defun inn-loop0 (amp)
  (proclaim '(type (pvar single-float) amp))

  ;;
  ;; Computation of the new value of the magnetic field along y
  ;;
  (*set reg (-!! (news!! e 0 1) e))

  ;;
  ;; Subtract off incident electric field
  ;;
  (*if boundary-north
    (*set reg (-!! reg (news!! beta 0 -1)))
  )

  ;;
  ;; The following operations are not required along the south
  ;; boundary (but applied anyways) since absorbing boundary
  ;; conditions are locally applied to the e field and hy is
  ;; determined by the outgoing plane wave condition.
  ;;
  (*set hy (!!! hy (!!! reg (!! gamma))))

  ;;
  ;; Computation of the new value of the magnetic field along x
  ;;
  (*set reg (-!! e (news!! e -1 0)))
  (*set hx (!!! hx (!!! (!! gamma) reg)))

  ;;
  ;; Computation of the electric field
  ;;
  ;; The allocation of the variables in our scheme requires a different
  ;; treatment of the south side of the domain to account for the
  ;; outgoing wave/absorbing boundary conditions.
  ;;
  (*set reg (-!! (news!! hx 1 0) hx))

  ;;
  ;; South boundary uses first order conditions for speed since
  ;; fields have not reached there yet.
  ;;
  (*if simulation-domain-not-north
    (*if boundary-south
      (*set reg (-!! reg (!!! (!! 2.0) (news!! hy 0 -1)))
      (*set reg (-!! (!!! reg hy) (news!! hy 0 -1)))
    )
  )

```

```

(prog ()
  (*set reg (!!! (!! c2) (-!! (news!! hx 0 1) (!!! reg (news!! hx 1 1))))
  (if (or ( numit 1) (> numit n_init))
    (prog ()
      (if (= numit 1)
        (setf tmp0 0.0)
        (setf tmp0 (* A (exp (- (expt (abs (/ (- (* (float (1- numit)) dt)
          (+ (/ (* kx dx) omega) t0) tt)) 2.0))))))
      )
      (*set reg (-!! (-!! (news!! e 0 1) (!!! amp (!! tmp0))) (!!! reg (!!! (!! c1) e)
    )
  )
  (prog ()
    (*set reg (-!! (-!! (news!! e 0 1) beta) (!!! reg (!!! (!! c1) e))))
  )
)
)

;;
;; Update of the incident electric field parameters.
;; If numit <= n_init apply gaussian; otherwise in
;; transition and introduce sinusoid
;;
(*if inc_fields
  (prog ()
    (if (> numit n_init)
      (prog ()
        (*set e (-!! (!!! alpha (!! gammaf)) (!!! beta (!! delta))))
        (*set beta (!!! (!!! beta (!! gammaf)) (!!! alpha (!! delta))))
        (*set alpha e)
      )
      (prog ()
        (*if dummy-layer-north
          (*set beta (!!! amp (!! (* A (exp (- (expt (abs (/ (- (* (float numit) dt)
            t0) tt)) 2.0))))))
          (*set beta (!!! amp (!! (* A (exp (- (expt (abs (/ (- (* numit dt)
            (+ (/ (* kx dx) omega) t0) tt)) 2.0))))))
          )
        )
      )
    )
    (*set e (!!! (!!! beta reg) (!!! e alpha)))
  )
)

;;
;; North boundary uses second order conditions
;;
(*if boundary-north
  (if (> numit n_init)
    (*set e (!!! reg (!!! (!! c1) (-!! (news!! e 0 1) (!!! amp (!!! (* A (exp
      (- (expt (abs (/ (- (* numit dt) (+ (/ (* kx dx) omega) t0) tt)) 2.0))))))))
    (*set e (!!! reg (!!! (!! c1) (-!! (news!! e 0 1) beta)))
  )
)
)

;;
;; end of the routine
;;

```